DISSERTATIONS IN
FORESTRY AND
NATURAL SCIENCES

Manisha Singh

Partially coherent beam shaping and imaging

Publications of the University of Eastern Finland
Dissertations in Forestry and Natural Sciences No 207

UNIVERSITY OF
EASTERN FINLAND

MANISHA SINGH

Partially coherent beam shaping and imaging

Publications of the University of Eastern Finland
Dissertations in Forestry and Natural Sciences
No 207

Academic Dissertation
To be presented by permission of the Faculty of Science and Forestry for public examination in the Auditorium M100 in Metria Building at the University of Eastern Finland, Joensuu, on December 11, 2015,
at 12 o'clock noon.

Institute of Photonics

Grano Oy
Jyväskylä, 2015
Editors: Prof. Pertti Pasanen, Prof. Kai Peiponen,
Prof. Pekka Kilpeläinen, Prof. Matti Vornanen

Distribution:
University of Eastern Finland Library / Sales of publications
julkaisumyynti@uef.fi
http://www.uef.fi/kirjasto

ISBN: 978-952-61-1998-4 (printed)
ISSNL: 1798-5668
ISSN: 1798-5668
ISBN: 978-952-61-1999-1 (pdf)
ISSNL: 1798-5668
ISSN: 1798-5676

Author's address:
University of Eastern Finland
Department of Physics and Mathematics
P. O. Box 111
FI-80101 JOENSUU
FINLAND
email: manisha.singh@uef.fi

Supervisors:
Professor Jari Turunen, Dr. Tech.
University of Eastern Finland
Department of Physics and Mathematics
P. O. Box 111
FI-80101 JOENSUU
FINLAND
email: jari.turunen@uef.fi

Associate Professor Jani Tervo, Ph.D.
University of Eastern Finland
Department of Physics and Mathematics
P. O. Box 111
FI-80101 JOENSUU
FINLAND
email: jani.tervo@gmail.com

Reviewers:
Professor Matti Kaivola, Dr. Tech.
Aalto University School of Science
Department of Applied Physics
P. O. Box 13500
FI-00076 AALTO
FINLAND
email: matti.kaivola@aalto.fi

Associate Professor Anna Burvall, Ph.D.
Royal Institute of Technology
Applied Physics Department
Roslagsvägen 30B
SE-114 19 STOCKHOLM
SWEDEN
email: anna.burvall@biox.kth.se

Opponent:
Professor Frank Wyrowski, Ph.D.
Friedrich-Schiller-Universität Jena
Institut für Angewandte Physik
Albert-Einstein-Strasse 15
D-07745 JENA
GERMANY
email: frank.wyrowski@uni-jena.de

ABSTRACT

The work summarized in this thesis contains analytical and numerical studies on the role of partial coherence of light in optical beam shaping and imaging systems. Spatially partially coherent stationary light fields as well as temporally and spectrally partially coherent non-stationary fields (pulse trains) are considered in the framework of classical second-order coherence theory. New methods for the analysis of beam shaping and imaging systems are developed, some of which are based on decomposing the partially coherent field into a set of fully coherent modal fields. The efficiency of such approaches is demonstrated by numerical examples.

Universal Decimal Classification: 535.1, 535.3, 535.4, 535.8
PACS Classification: 42.15.Eq, 42.25.Kb, 42.30.Kq, 42.25.Gy, 42.15.Fr, 42.30.Lr
Keywords: optics; light; light diffraction; light coherence; imaging; high-speed optical techniques; micro-optics
Yleinen suomalainen asiasanasto: optiikka; valo; koherenssi; kuvantaminen

Preface

I feel really privileged to be defending my thesis in the International Year of Light. I always believed that the process of learning never ends and I am still learning. This thesis sums up the learning, I did as a researcher. My scientific journey includes several people that I would like to acknowledge. Firstly, I would like to express my gratitude to my supervisors Prof. Jari Turunen, Assoc. Prof. Jani Tervo and my co-author Hanna Lajunen who have encouraged and inspired me in this work. They have helped me to become an independent scientist, which I really appreciate.

I am also grateful to my reviewers of this thesis, Prof. Matti Kaivola and Assoc. Prof. Anna Burvall. Their positive comments and suggestions have been valuable in writing this thesis. I would like to appreciate Prof. Frank Wyrowski who has promised to be my opponent.

I am also thankful to Prof. Seppo Honkanen, Prof. Jyrki Saarinen and Prof. Pasi Vahimaa for giving good advice during my studies. I would like to thank Hannele Karpinen for supporting me through the emotional phases of my life. I would also give my regards to my friends Ali Rizwan, Bisrat Asefa, Bhabishya Gurung, Henri Partanen, Manash Shah, Paras Pant, Prakash Pokhrael, Rahul Dutta and Vishal Gandhi for making this journey lively and for providing continuous motivation during my thesis.

Last, but certainly not least, I wish to thank my parents and siblings for their support. Most importantly, I would like to give my heartfelt thanks to Anup Nepal, my husband for supporting me in my ups and downs and believing in me.

My deepest gratitude to all of you who have been a guiding light in my pursuit.

Joensuu Nov 6, 2015 *Manisha Singh*

LIST OF PUBLICATIONS

This thesis consists of the present review of the author's work in the field of optical coherence theory and diffractive optics, and the following selection of the author's publications:

I M. Singh, J. Tervo, and J. Turunen, "Elementary-field analysis of partially coherent beam shaping," *J. Opt. Soc. Am. A* **30,** 2611–2617 (2013).

II M. Singh, J. Tervo, and J. Turunen, "Broadband beam shaping with harmonic diffractive optics," *Opt. Express* **22,** 22680–22688 (2014).

III M. Singh, H. Lajunen, J. Tervo, and J. Turunen, "Spatial shaping of spectrally partially coherent pulsed beams," *Opt. Express* **23,** 12680–12691 (2015).

IV M. Singh, H. Lajunen, J. Tervo, and J. Turunen, "Imaging with partially coherent light: elementary-field approach," *Opt. Express* **23,** 28132–28140 (2015).

Throughout the overview, these papers will be referred to by Roman numerals.

Some of the results have been presented by the author in international conferences:

1. Days on Diffraction 13, (St.Petersburg, Russia, 2013, poster). M. Singh, J. Tervo, and J. Turunen,"Diffractive homegenizing of spatially partially coherent beams".

2. ICO–23, (Santiago de Compostela, Spain, 2014, oral presentation). M. Singh, "Elementary-field representation of spatially partially coherent beams in optical system".

3. EOSAM 2014, (Berlin Adlershof, Germany, 2014, oral presentation). M. Singh, "Comparative study of refractive and diffractive homogenizers for broadband pulses".

4. SPIE Optical Systems Design 2015, (Jena, Germany, 2015, poster and paper), M. Singh, H. Lajunen, J. Tervo, and J. Turunen, "Beam shaping of supercontinuum pulses," *Proc. SPIE* **9626,** 331–336 (2015), doi:10.1117/12.2191264.

AUTHOR'S CONTRIBUTION

The publications selected in this dissertation are original research papers, which are results of group efforts. In all publications the author has performed most of the analytical calculations and all numerical simulations. The author has participated in writing all manuscripts to the papers **I**–**IV** and had an active role in developing ideas that lead to these publications.

Contents

1 Introduction

Optical fields are often idealized as being strictly harmonic (monochromatic) waves or deterministic wave packets (pulses) that consist of a continuum of mutually correlated frequency components. In the case of stationary fields, single-mode laser beams represent the ideal case of full spatial coherence, allowing light waves emanating from different points of space to interfere. Correspondingly, single-mode femtosecond lasers produce fully coherent pulse trains in the sense that all pulses are of identical spectral and temporal form. However, all real stationary or pulsed electromagnetic fields undergo certain fluctuations either in the spatial, temporal, or frequency domains, or in all of them. Not even single-mode lasers are fully stable, and femtosecond pulse trains produced by mode-locked lasers exhibit some pulse-to-pulse variations. Such fluctuations are, in general, best treated by considering the optical field as a random process and applying statistical methods to describe it. This is all the more important if one considers stationary sources of light such as thermal emitters and light-emitting diodes, in which the spatial correlations of light fields emitted from two closely spaced points is low. Similarly, a statistical description is a natural approach to describe pulse trains in which the individual pulses have non-identical wave forms. Optical coherence theory of stationary [1–4] and non-stationary [5–7] fields describes correlations between field fluctuations at two (or more) points in the spatial, angular, temporal, or spectral regime, and forms the basis of the work reported in this thesis.

Both beam shaping and imaging problems with partially coherent light will be considered. In beam shaping, the goal is to transform a field with a given spatial profile (typically Gaussian) into some other predefined profile [8–14], which is often an approximation of a flat-top profile [15]. This task can, in general, be accomplished either with refractive free-form elements [16–23]

or by means of diffractive elements [24–32] with an appropriately designed phase transmission function [33], or with so-called harmonic diffractive elements [34–39], which provide a transition between purely diffractive elements and refractive elements. These different types of elements are equivalent for monochromatic light, but their chromatic properties differ widely [40–42] and this becomes important if one considered the shaping of ultrashort pulses with broadband spectra. Also non-perfect spatial coherence has an effect in the performance of beam shaping elements since the spreading properties of optical beams depend critically on the spatial coherence of the source [43–45]. All of these aspects will be considered in this thesis and in Papers I–III.

In the case of partially coherent fields, propagation integrals of spatial correlation functions are generally four-dimensional (4D), which makes their numerical treatment more or less untractable. In order to make numerical calculations feasible, so-called modal approaches [46–51] are used extensively, especially to describe partial spatial coherence. Such modal approaches, in which the partially coherent field is represented as a superposition of fully coherent fields, lead to the evaluation of a set of two-dimensional (2D) integrals instead of a single 4D integral. Modal decompositions offer great benefits in numerical treatment of partially coherent light in, e.g., beam shaping problems. In this thesis they are also applied to imaging problems (Paper IV) and shown to facilitate efficient analysis of these problems regardless of the degree of spatial coherence of object illumination.

The thesis is organized as follows.

In Chapter 2, the basic concepts of optical coherence theory are presented, which are applicable to stationary and non-stationary scalar fields. The correlation functions in the space-time and space-frequency domains are introduced, and the coherence properties of several partially coherent light sources are discussed in brief.

In Chapter 3, we focus on beam shaping by refractive, diffractive, and hybrid optical elements. This chapter also includes the basic concepts of the optical map transform method. The designed

beam shaping elements are then considered assuming illumination by broadband light sources. The performance of all three types of beam shaping elements are compared using examples (frequency-integrated results).

In Chapter 4, two different modal approaches, namely the Mercer coherent-mode representation and the elementary field representation [52,53], are presented in the form applicable to stationary and non-stationary fields. These modal decomposition techniques are applied to Gaussian Schell-model beams and pulses. Examples of this kind of models are discussed.

In Chapter 5, we deal with one of the most prohibitive numerical problems in optics, i.e., image formation with spatially partially coherent light. The traditional theoretical approaches involve four-dimensional integrals, the numerical evaluation of which is a prohibitive task especially for objects of complicated structure. With the help of the elementary-field representation, we introduce an efficient and computationally feasible method, which is discussed with examples on bright-field and dark-field imaging geometries.

Finally, in Chapter 6, the main conclusions of this work and some future prospects are presented.

2 Coherence of stationary and non-stationary fields

There are numerous randomly radiating but temporally stationary primary light sources, such as thermal sources, whose statistical properties are time-invariant. This kind of random sources can be best described using the optical coherence theory of light [1], which is based on correlation functions obtained either by calculating time averages of certain products of field quantities or averages over ensembles formed by individual field realizations. On the other hand, there are numerous non-stationary sources including mode-locked femtosecond lasers, supercontinuum sources, and free-electron lasers, which produce trains of short pulses. In this case subsequent pulses in the train can be considered as individual field realizations, which may be more or less identical. Correlation functions that describe the statistical properties of the pulse train can be defined by means of ensemble averages of products of field quantities in analogy with the stationary case [5–7]. Coherence properties of optical fields can be characterized by means of these correlation functions.

Both stationary and non-stationary sources, and the fields radiated by them, can be spatially and temporally fully or partially coherent. In the case of stationary sources (and fields), the temporal coherence is a function of only the time difference $\tau = t_2 - t_1$ (one time coordinate), while the temporal coherence properties of non-stationary sources must be described by a correlation function that depends on both t_1 and t_2 (two time coordinates). Similarly, there is an important difference between stationary and non-stationary sources if their spectral correlations are considered. In the case of stationary fields, all frequency components of light are strictly uncorrelated and hence the spectral-domain correlation function de-

pends on only one frequency coordinate. In the non-stationary case, any (full or partial) degree of correlation between two frequencies ω_1 and ω_2 is generally possible.

In this thesis both stationary and non-stationary light sources and fields are considered. However, although the electromagnetic field is vectorial in nature, the studies presented here are restricted to scalar fields. Ignoring the vectorial nature of the field amounts to neglecting important phenomena like polarization, but this is often acceptable especially in the paraxial domain, where only the two transverse components of the electric field are significant and can be treated independently.

In this chapter the qualitative considerations presented above are put on a firm mathematical basis by formally introducing the correlations functions used in the scalar description of both stationary and non-stationary fields. We begin with a complex representation of the optical field itself and proceed to a formal description of field correlations in space-time and space-frequency domains. Finally, spatial, spectral, and temporal correlation properties of some typical partially coherent light sources are described in a qualitative fashion.

2.1 BASIC FIELD REPRESENTATION

Monochromatic harmonic fields are real, but it is customary to use a complex representation because of its mathematical convenience. A complex representation is convenient also for polychromatic fields. It leads to the concept of a complex analytic signal [54] and to a Fourier-transform relationship between field representations in time and frequency domains.

Let us consider a scalar field $V_{\mathrm{re}}(\boldsymbol{r}, t)$, which is a real-valued function of position $\boldsymbol{r}$ and time t and satisfies the wave equation in vacuum. This function can be represented as a Fourier integral

$$V_{\mathrm{re}}(\boldsymbol{r}, t) = \int_{-\infty}^{\infty} V(\boldsymbol{r}, \omega) \exp\left(-\mathrm{i}\omega t\right) \mathrm{d}\omega, \tag{2.1}$$

where the field is decomposed into its components at different angular frequencies ω.

Since the field $V_{\mathrm{re}}(\boldsymbol{r}, t)$ is real, the negative frequency components contain no information that is not already present in the positive frequency components. Thus the field is completely specified by the complex analytic signal defined as

$$V(\boldsymbol{r}, t) = \int_0^\infty V(\boldsymbol{r}, \omega) \exp\left(-\mathrm{i}\omega t\right) \mathrm{d}\omega, \tag{2.2}$$

where, by inverse Fourier transform,

$$V(\boldsymbol{r}, \omega) = \frac{1}{2\pi} \int_{-\infty}^\infty V(\boldsymbol{r}, t) \exp\left(\mathrm{i}\omega t\right) \mathrm{d}t. \tag{2.3}$$

This mathematically convenient complex field representation will be employed throughout the thesis.

2.2 MUTUAL COHERENCE FUNCTION

In the space-time domain the second-order coherence properties of the field are characterized by a correlation function that generally depends on two arbitrary spatial positions $\boldsymbol{r}_1$ and $\boldsymbol{r}_2$, and on two arbitrary instants of time t_1 and t_2. If the field is stationary, its statistical properties are independent of the origin of time and the correlations therefore depend only on the time difference $\tau = t_2 - t_1$. Th appropriate correlation function is then the Mutual Coherence Function (MCF) defined as

$$\Gamma(\boldsymbol{r}_1, \boldsymbol{r}_2, \tau) = \langle V^*(\boldsymbol{r}_1, t) V(\boldsymbol{r}_2, t + \tau) \rangle. \tag{2.4}$$

Here the angular brackets may be interpreted as the time average over the quantity enclosed, i.e.,

$$\langle V^*(\boldsymbol{r}_1, t) V(\boldsymbol{r}_2, t + \tau) \rangle = \lim_{T \to \infty} \frac{1}{T} \int_{-T/2}^{T/2} V^*(\boldsymbol{r}_1, t) V(\boldsymbol{r}_2, t + \tau) \, \mathrm{d}t. \tag{2.5}$$

Alternatively, one may consider a set (ensemble) of field realizations $V_n(\boldsymbol{r}, t)$ (long but finite temporal sections of the field) and define an

ensemble average

$$\langle V^*(\boldsymbol{r}_1,t)V(\boldsymbol{r}_2,t+\tau)\rangle = \lim_{N\to\infty}\frac{1}{N}\sum_{n=1}^{N} V_n^*(\boldsymbol{r}_1,t)V_n(\boldsymbol{r}_2,t+\tau). \quad (2.6)$$

Very often these two definitions produce the same result, and in this case the field is said to be ergodic.

It is convenient to define a normalized form of the MCF, known as the complex degree of coherence, by the formula

$$\gamma(\boldsymbol{r}_1,\boldsymbol{r}_2,\tau) = \frac{\Gamma(\boldsymbol{r}_1,\boldsymbol{r}_2,\tau)}{[\boldsymbol{I}(\boldsymbol{r}_1)\boldsymbol{I}(\boldsymbol{r}_2)]^{1/2}}, \quad (2.7)$$

where

$$I(\boldsymbol{r}) = \Gamma(\boldsymbol{r},\boldsymbol{r},0) = \langle |V(\boldsymbol{r},t)|^2\rangle \quad (2.8)$$

represents the spatial intensity distribution of the field. The function $\gamma(\boldsymbol{r}_1,\boldsymbol{r}_2,\tau)$ satisfies the inequalities

$$0 \le |\gamma(\boldsymbol{r}_1,\boldsymbol{r}_2,\tau)| \le 1, \quad (2.9)$$

where the lower limit represents complete incoherence and the upper limit full coherence of field fluctuations at points $\boldsymbol{r}_1$ and $\boldsymbol{r}_2$, and at time delay τ. Spatial coherence is characterized by zero-time-delay functions $\Gamma(\boldsymbol{r}_1,\boldsymbol{r}_2,0)$ and $\gamma(\boldsymbol{r}_1,\boldsymbol{r}_2,0)$, while temporal coherence at any single point $\boldsymbol{r}$ is characterized by functions $\Gamma(\boldsymbol{r},\boldsymbol{r},\tau)$ and $\gamma(\boldsymbol{r},\boldsymbol{r},\tau)$.

In addition to stationary fields, also pulse trains are considered in this thesis. In the case of such non-stationary fields the correlations depend on both temporal coordinates and the MCF is defined as

$$\Gamma(\boldsymbol{r}_1,\boldsymbol{r}_2,t_1,t_2) = \langle V^*(\boldsymbol{r}_1,t_1)V(\boldsymbol{r}_2,t_2)\rangle. \quad (2.10)$$

Here different pulses are considered as field realizations and the angular brackets denote an ensemble average

$$\langle V^*(\boldsymbol{r}_1,t_1)V(\boldsymbol{r}_2,t_2)\rangle = \lim_{T\to\infty}\frac{1}{N}\sum_{n=1}^{N} V^*(\boldsymbol{r}_1,t_1)V(\boldsymbol{r}_2,t_2). \quad (2.11)$$

In analogy with the stationary case, the spatiotemporal intensity distribution is defined by setting $\boldsymbol{r}_1 = \boldsymbol{r}_2 = \boldsymbol{r}$ and $t_1 = t_2 = t$ in Eq. (2.11), which gives

$$I(\boldsymbol{r}, t) = \Gamma(\boldsymbol{r}, \boldsymbol{r}, t, t) = \langle |V(\boldsymbol{r}, t)|^2 \rangle. \tag{2.12}$$

The normalized form of MCF, still called the complex degree of coherence, is defined as

$$\gamma(\boldsymbol{r}_1, \boldsymbol{r}_2, t_1, t_2) = \frac{\Gamma(\boldsymbol{r}_1, \boldsymbol{r}_2, t_1, t_2)}{[\boldsymbol{I}(\boldsymbol{r}_1, t_1)\boldsymbol{I}(\boldsymbol{r}_2, t_2)]^{1/2}} \tag{2.13}$$

and it obeys the inequalities

$$0 \leq |\gamma(\boldsymbol{r}_1, \boldsymbol{r}_2, t_1, t_2)| \leq 1, \tag{2.14}$$

where the lower and upper bounds represent complete incoherence and complete coherence between the two space-time points, respectively.

2.3 CROSS-SPECTRAL DENSITY FUNCTION

In addition to field correlations in the space-time domain, it is of interest to examine correlations in the space-frequency domain, i.e., as a function of two spatial coordinates $\boldsymbol{r}_1$ and $\boldsymbol{r}_2$ and two frequencies ω_1 and ω_2. In many instances it is more natural and mathematically simpler to consider fields in this domain. This is true, for example, in propagation, beam shaping, and imaging problems considered later on in this thesis.

The precise theory of coherence of stationary optical fields in the space-frequency domain was developed by Wolf [46,47,55]. The central quantity in this theory is the cross-spectral density function (CSD), defined by means of the spectral field representation $V(\boldsymbol{r}, \omega)$ introduced in Eq. (2.3).

Considering non-stationary fields first, the CSD is defined as an ensemble average

$$W(\boldsymbol{r}_1, \boldsymbol{r}_2, \omega_1, \omega_2) = \langle V^*(\boldsymbol{r}_1, \omega_1) V(\boldsymbol{r}_2, \omega_2) \rangle. \tag{2.15}$$

In analogy with the quantities in the space-time domain, we define the spectral density of the field, or the power spectrum at position $\boldsymbol{r}$, as

$$S(\boldsymbol{r},\omega) = W(\boldsymbol{r},\boldsymbol{r},\omega,\omega) = \langle |V(\boldsymbol{r},\omega)|^2 \rangle. \tag{2.16}$$

Further, it is useful to define a normalized form of the CSD as

$$\mu(\boldsymbol{r}_1,\boldsymbol{r}_2,\omega_1,\omega_2) = \frac{W(\boldsymbol{r}_1,\boldsymbol{r}_2,\omega_1,\omega_2)}{\sqrt{S(\boldsymbol{r}_1,\omega_1)S(\boldsymbol{r}_2,\omega_2)}}. \tag{2.17}$$

This quantity, called the complex degree of spectral coherence, satisfies the inequalities

$$0 \leq |\mu(\boldsymbol{r}_1,\boldsymbol{r}_2,\omega_1,\omega_2)| \leq 1. \tag{2.18}$$

The lower and upper bounds correspond to complete incoherence and coherence, respectively, between field fluctuations at the two space-frequency points. Spatial coherence at any given frequency ω is characterized by functions $W(\boldsymbol{r}_1,\boldsymbol{r}_2,\omega,\omega)$ and $\mu(\boldsymbol{r}_1,\boldsymbol{r}_2,\omega,\omega)$, while spectral coherence at a spatial point $\boldsymbol{r}$ is characterized by functions $W(\boldsymbol{r},\boldsymbol{r},\omega_1,\omega_2)$ and $\mu(\boldsymbol{r},\boldsymbol{r},\omega_1,\omega_2)$.

By inserting from Eqs. (2.3) and (2.10) into Eq. (2.15) we immediately find that

$$W(\boldsymbol{r}_1,\boldsymbol{r}_2,\omega_1,\omega_2) = \frac{1}{(2\pi)^2} \iint_{-\infty}^{\infty} \Gamma(\boldsymbol{r}_1,\boldsymbol{r}_2,t_1,t_2) \times \exp\left[-\mathrm{i}\left(\omega_1 t_1 - \omega_2 t_2\right)\right] \mathrm{d}t_1\,\mathrm{d}t_2 \tag{2.19}$$

and, inversely,

$$\Gamma(\boldsymbol{r}_1,\boldsymbol{r}_2,t_1,t_2) = \iint_{0}^{\infty} W(\boldsymbol{r}_1,\boldsymbol{r}_2,\omega_1,\omega_2) \times \exp\left[\mathrm{i}\left(\omega_1 t_1 - \omega_2 t_2\right)\right] \mathrm{d}\omega_1\,\mathrm{d}\omega_2. \tag{2.20}$$

This connection between the CSD and MCF is called the generalized Wiener–Khintchine theorem for non-stationary fields [56–61].

Let us proceed to consider stationary fields by assuming that the MCF has the form of Eq. (2.4) and insert $t_1 = t$, $t_2 = t + \tau$ into

Eq. (2.19). Defining

$$W(\boldsymbol{r}_1, \boldsymbol{r}_2, \omega) = \frac{1}{2\pi} \int_{-\infty}^{\infty} \Gamma(\boldsymbol{r}_1, \boldsymbol{r}_2, \tau) \exp(\mathrm{i}\omega\tau)\ \mathrm{d}\tau \tag{2.21}$$

we get the relation

$$W(\boldsymbol{r}_1, \boldsymbol{r}_2, \omega_1, \omega_2) = W(\boldsymbol{r}_1, \boldsymbol{r}_2, \omega_1)\delta(\omega_1 - \omega_2), \tag{2.22}$$

which shows that all frequency components of a stationary field are uncorrelated. The CSD of a stationary field, defined according to Eq. (2.22), is related to the MCF though Eq. (2.21) and its inverse

$$\Gamma(\boldsymbol{r}_1, \boldsymbol{r}_2, \tau) = \int_0^{\infty} W(\boldsymbol{r}_1, \boldsymbol{r}_2, \omega) \exp(-\mathrm{i}\omega\tau)\ \mathrm{d}\omega. \tag{2.23}$$

These equations constitute the generalized Wiener–Khintchine theorem for stationary light.

The spectral density of a stationary field is defined as $S(\boldsymbol{r}, \omega) = W(\boldsymbol{r}, \boldsymbol{r}, \omega)$ and its complex degree of coherence by an expression analogous to Eq. (2.17),

$$\mu(\boldsymbol{r}_1, \boldsymbol{r}_2, \omega) = \frac{W(\boldsymbol{r}_1, \boldsymbol{r}_2, \omega)}{\sqrt{S(\boldsymbol{r}_1, \omega) S(\boldsymbol{r}_2, \omega)}}. \tag{2.24}$$

We now have the inequalities $0 \leq |\mu(\boldsymbol{r}_1, \boldsymbol{r}_2, \omega)| \leq 1$ and the Fourier-transform relations

$$S(\boldsymbol{r}, \omega) = \frac{1}{2\pi} \int_{-\infty}^{\infty} \Gamma(\boldsymbol{r}, \boldsymbol{r}, \tau) \exp(\mathrm{i}\omega\tau)\ \mathrm{d}\tau, \tag{2.25}$$

$$\Gamma(\boldsymbol{r}, \boldsymbol{r}, \tau) = \int_0^{\infty} S(\boldsymbol{r}, \omega) \exp(-\mathrm{i}\omega\tau)\ \mathrm{d}\omega \tag{2.26}$$

between the spectral density and the autocorrelation function of a stationary random process. These relations form the (standard) Wiener–Khintchine theorem [62–64] and they provide an important connection between the spectrum and the temporal coherence function of stationary light.

2.4 PARTIALLY COHERENT LIGHT SOURCES

Before having a closer look at the mathematical models and the modal approaches that can be used to describe different types of real light sources, it is necessary to understand the coherence properties of these sources. When the spectral content is considered, a source can be considered as monochromatic (single frequency), quasi-monochromatic (spectral bandwidth is much smaller than the mean frequency), or polychromatic (the spectral bandwidth is significant compared to the center frequency). Only stationary sources (in practise single-mode lasers) can be approximated as being monochromatic since, according to Eq. (2.3), short pulses necessarily have frequency spectra of finite bandwidth [65].

Considering spatial coherence, a stationary source is fully coherent in the space-frequency domain if the CSD can be represented in a factored form $W(\boldsymbol{r}_1, \boldsymbol{r}_2, \omega) = V^*(\boldsymbol{r}_1, \omega)V(\boldsymbol{r}_2, \omega)$, which implies that $|\mu(\boldsymbol{r}_1, \boldsymbol{r}_2, \omega)| = 1$ [66]. Correspondingly, it is fully spatially coherent in space-time domain if $\Gamma(\boldsymbol{r}_1, \boldsymbol{r}_2, 0) = V^*(\boldsymbol{r}_1, t)V(\boldsymbol{r}_2, t)$ and hence $|\gamma(\boldsymbol{r}_1, \boldsymbol{r}_2, 0)| = 1$. It should be noted that even if the source (or field) is fully spatially coherent at every frequency ω, it is not necessarily fully coherent in the space-time domain [67]. This is the case, for example, if the transverse scale or shape of $S(\boldsymbol{r}, \omega)$ of a stationary field depends on ω [68, 69].

If we consider a source that emits light predominantly in the z direction and assume that $\boldsymbol{r}_1$ and $\boldsymbol{r}_2$ are located in the source plane, the spatial coherence area of the source is the region in which $|\mu(\boldsymbol{r}_1, \boldsymbol{r}_2, \omega)|$ or $|\gamma(\boldsymbol{r}_1, \boldsymbol{r}_2, 0)|$ (depending on whether we consider the field in the spcae-frequency or in the space-time domain) differs significantly from zero. Generally, the coherence area is space-variant in the sense that it depends on the center coordinate $\boldsymbol{r} = \frac{1}{2}(\boldsymbol{r}_1 + \boldsymbol{r}_2)$. However, many sources are at least approximately of the Schell-model form, such that μ or γ depend only on the coordinate difference $\Delta\boldsymbol{r} = \boldsymbol{r}_2 - \boldsymbol{r}_1$, and in this case the coherence area is space-invariant.

If the spatial coherence area is everywhere comparable to, or

larger than the effective area of $S(\boldsymbol{r},\omega)$ or $I(\boldsymbol{r})$, one speaks of a quasi-coherent source in space-frequency and space-time domains, respectively. If, on the other hand, the coherence area is everywhere small compared to the source size, one customarily uses the term quasihomogeneous source. Similar terms are used also for fields radiated by primary sources. An incoherent source is obtained in the limit of zero coherence area. However, this is an idealization (though often a quite useful one). It can be shown that the smallest possible dimensions of the coherence area are of the order of the wavelength [70]. In fact, even if the coherence area of a primary source were in the subwavelength scale, the coherence area of the field radiated by it would grow to wavelength scale after a propagation distance of only a few wavelengths since at that distance the evanescent spatial-frequency components of the field die out.

Similar terminology (quasi-coherence and quasi-homogeneity) is applicable to spatial coherence of non-stationary sources. The only difference is that one considers the function $\mu(\boldsymbol{r}_1,\boldsymbol{r}_2,\omega,\omega)$ instead of $\mu(\boldsymbol{r}_1,\boldsymbol{r}_2,\omega)$, and $\gamma(\boldsymbol{r}_1,\boldsymbol{r}_2,t,t)$ instead of $\gamma(\boldsymbol{r}_1,\boldsymbol{r}_2,0)$, when defining the coherence area.

As already seen from Eq. (2.22), a strictly stationary source is always spectrally incoherent, i.e., all of its frequency components are uncorrelated. Such a source is fully temporally coherent at point $\boldsymbol{r}$ if $|\gamma(\boldsymbol{r},\boldsymbol{r},\tau)| = 1$ for all τ and temporally partially coherent if $|\gamma(\boldsymbol{r},\boldsymbol{r},\tau)|$ has a finite effective width (coherence time). It should be noted that no temporally incoherent sources exist since the $\Gamma(\boldsymbol{r},\boldsymbol{r};\tau)$ is related to the spectrum $S(\omega)$ through the Wiener–Khintchine theorem (2.25); since $S(\omega)$ has a finite bandwidth, its Fourier transform $\Gamma(\boldsymbol{r},\boldsymbol{r};\tau)$ must have a finite temporal width.

Non-stationary sources (and fields) are fully spatially and spectrally coherent if the two-frequency CSD is of the factored form $W(\boldsymbol{r}_1,\boldsymbol{r}_2,\omega_1,\omega_2) = V^*(\boldsymbol{r}_1,\omega_1)V(\boldsymbol{r}_2,\omega_2)$, which immediately implies that $|\mu(\boldsymbol{r}_1,\boldsymbol{r}_2,\omega_1,\omega_2)| = 1$. Similarly, non-stationary sources are fully spatially and temporally coherent if the two-time MCF can be represented as $\Gamma(\boldsymbol{r}_1,\boldsymbol{r}_2,t_1,t_2) = V^*(\boldsymbol{r}_1,t_1)V(\boldsymbol{r}_2,t_2)$, which implies that $|\gamma(\boldsymbol{r}_1,\boldsymbol{r}_2,t_1,t_2)| = 1$. This type of fields are generated, to an

excellent approximation, by mode-locked lasers [71].

Considering the field at a single point $\boldsymbol{r}_1 = \boldsymbol{r}_2 = \boldsymbol{r}$, the spectral coherence area is defined as the effective region within which $|\mu(\boldsymbol{r}_1, \boldsymbol{r}, \omega_1, \omega_2)|$ differs significantly from zero, and the temporal coherence area is the region where $|\gamma(\boldsymbol{r}_1, \boldsymbol{r}_2, t_1, t_2)|$ has significant values. In general, the spectral coherence area depends on the mean frequency $\omega = \frac{1}{2}(\omega_1 + \omega_2)$ and the temporal coherence area is a function of the mean time $t = \frac{1}{2}(t_1 + t_2)$. However, often one can assume that $|\mu(\boldsymbol{r}, \boldsymbol{r}, \omega_1, \omega_2)| = |\mu(\boldsymbol{r}, \boldsymbol{r}, \Delta\omega)|$ with $\Delta\omega = \omega_2 - \omega_1$, i.e., the field is spectrally of the Schell-model form. In this case the spectral coherence area depends only on the frequency difference $\Delta\omega$ and not on the mean frequency ω. Similarly, if the field is temporally of the Schell-model form, the temporal coherence area depends only on $t_2 - t_1$.

In full analogy with spatial coherence, a non-stationary field is spectrally quasi-coherent if the dimensions of the spectral coherence area of the same order of magnitude as the mean spectral width, and a corresponding criterion defines temporally quasi-coherent fields. Non-stationary fields are called quasi-stationary if the temporal coherence area is small compared to the pulse duration, which typically implies that also the spectral coherence area is small compared to the spectral width. In general, if we fix the spectral width and reduce the spectral coherence area, the pulse duration increases. In reverse, if we consider pulses of fixed duration and reduce the temporal coherence area, the spectrum widens. As with stationary fields, no temporally incoherent pulsed fields exist.

Continuous-wave (CW) single-mode lasers (He-Ne, Nd:YAG, Ar^+, etc.) are, for nearly all practical purposes, fully spatially and temporally coherent. As already mentioned, mode-locked femtosecond lasers are virtually fully coherent spatially, spectrally, and temporally. However, all other sources are partially coherent in at least one of these domains. Let us next consider some examples of such partially coherent sources.

As stated above, there are no strictly spatially incoherent sources

but thermal sources and surface-emitting LEDs have spatial coherence areas with dimensions of the order of the wavelength and are therefore quasihomogeneous. However, if light from such a source is collimated, one creates a virtual source with an increased apparent coherence area. In the case of quasihomogeneous sources, the divergence of the field is inversely proportional to the coherence area instead of the source size as it is in the case of fully spatially coherent fields [72]. Hence, the better the field is collimated, the larger is the apparent coherence area.

The temporal coherence properties of thermal sources and LEDs operating in the continuous-wave mode differ quite significantly. Thermal sources are broadband emitters, thus having very short (femtosecond-range) coherence times, while LEDs are polychromatic but nevertheless rather narrow-band sources, thus having significantly larger coherence times [73]. Of course, spectral filtering of a thermal source increases the coherence time according to the passband of the filter as dictated by the Wiener–Khintchine theorem.

Laser diodes operating in a single transverse and longitudinal mode are good approximations of fully spatially and temporally coherent sources. However, to obtain a high output power from a single diode laser requires that a large number of transverse and longitudinal modes are allowed to be excited. Broad-area laser diodes (BALDs) with high output power are stationary, quasimonochromatic, quasi-homogeneous, and temporally partially coherent light sources [74–80]. Even higher power levels can be achieved by means of arrays of vertical-cavity surface-emitting lasers [81, 82]. Depending on the way of construction, individual lasers in such arrays can be coupled in order to produce nearly spatially coherent illumination (which however is highly structured), or the adjacent lasers may emit light independently from each other [83, 84]. In the latter case, the array behaves as a quasimonochromatic spatially partially coherent source.

There are also several pulsed sources with different coherence states. Excimer lasers are pulsed sources operating in the ultravi-

olet region of the spectrum, which have important applications in, e.g., optical projection lithography and biomedical optics [85–89]. These lasers can be characterized as quasi-monochromatic, quasi-homogeneous and quasi-stationary light sources.

Supercontinuum (SC) light sources realized by pumping nonlinear optical fibers with pulsed light produce highly broadband (even octave-band) fields. These sources are spatially fully coherent in the spectral domain and spatially quasi-coherent in the temporal domain. The spectral and temporal coherence properties vary widely depending on the pump pulse power and duration [90–95]. It has been recently demonstrated that the two-frequency CSD and the two-time MCF contain both quasi-coherent and quasi-stationary contributions (the spectral coherence width varies widely as a function of ω and the coherence time varies with t) [93].

Finally, X-Ray Free-Electron Lasers (XFELs) [96, 97] are quasi-monochromatic sources of short-wavelength radiation. Beams radiated by these sources have been unambiguously demonstrated as being spatially quasi-coherent [98]. The temporal coherence properties of XFELs have also been studied and they have been shown to be partial [99–106]. There are indications that some XFELs are temporally quasi-coherent, while others are quasi-stationary.

3 Broadband beam shaping

In this chapter we study the effects of a finite spectral width of the illuminating field in beam shaping problems, which are relevant in, e.g., target illumination, imaging, laser printing, beam homogenization, and holography [107–111]. The idea is to use a specially designed element to modulate the phase of the incident beam in such a way that a desired intensity distribution is obtained either in the Fresnel region or in the far field. In particular, we consider elements designed by the optical map transform method [28,112–114], although there exist many other ways of designing beam shaping elements [115–118], including the iterative Fourier-transform algorithm [109,119,120].

Elements designed by the geometrical map-transform method can be realized in different forms, such as diffractive or refractive surface-relief structures, modulo $2\pi M$ (M = integer) diffractive structures that are generalizations of harmonic diffractive lenses [121, 122], or hybrid structures that are combinations of refractive and diffractive elements [34, 35]. The performance of these different types of element is compared in Paper II, with a summary provided below. It is a common belief that purely diffractive elements work appropriately only for quasimonochromatic light fields with narrow frequency spectra, though previous studies indicate that they can be used to shape beams from wavelength-tunable lasers [123, 124]. The simulation results given below show that purely diffractive elements can perform surprisingly well even if extremely wide-bandwidth light beams from either stationary (such as thermal or RGB, Red/Green/Blue) sources or ultra-wide-bandwidth pulsed supercontinuum light sources are considered.

3.1 THE GEOMETRICAL MAP TRANSFORM METHOD

The principles of the optical map transform method were introduced independently by Kurtz *et al.* [112] and Bryngdahl [113]. The basis of this method is a geometrical energy conservation (or balance) criterion, which relates the energy distributions at the input (element) and the output (target) planes as schematically illustrated in Fig. 3.1.

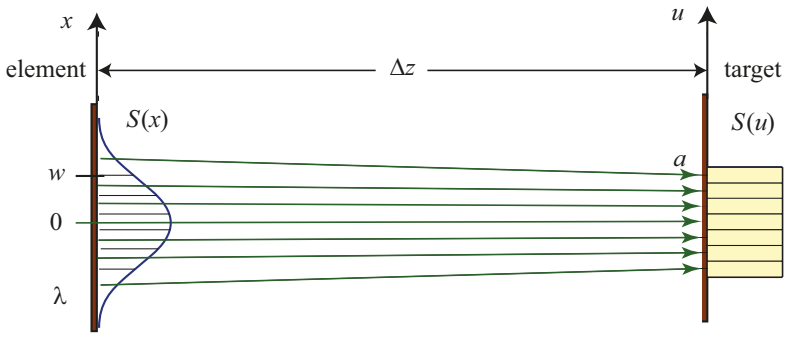

Figure 3.1: The principle of the geometrical map-transform method in a y-invariant geometry, illustrated for Gaussian to flat-top transformation in a discrete form. The intensity distributions at the element and target planes are divided into sections of equal energy, and the task of the element is to redirect the incident field in such a way that these sections are connected.

Assuming first monochromatic illumination at some frequency ω_0 (and wavelength $\lambda_0 = 2\pi c/\omega_0$), which we ignore from notation for the time being, we denote the field incident on the element by $V(x)$ and its intensity (spectral density) by $S(x)$, normalized such that $\int_{-\infty}^{\infty} S(x)\,\mathrm{d}x = 1$. Within the usual thin-element approximation [125], the action of the element is described by a phase-only complex-amplitude transmission function $t(x) = \exp[\mathrm{i}\phi(x)]$. The goal is to design the phase function $\phi(x)$ in such a way that the target-plane intensity distribution has a prescribed form $S(u)$, which satisfies $\int_{-\infty}^{\infty} S(u)\,\mathrm{d}u = 1$ (energy conservation).

If we let the finite sections of equal energy in the element and target planes of Fig. 3.1 become infinitely narrow, we arrive at a mapping $x \to u(x)$ between the ray exit point x at the element

plane and the ray arrival point $u(x)$ at the target plane, which can be determined from the energy balance condition

$$\int_0^x S(x')\,\mathrm{d}x' = \int_0^{u(x)} S(u')\,\mathrm{d}u'. \tag{3.1}$$

In writing this expression we have assumed mirror symmetries $S(-x) = S(x)$ and $S(-u) = S(u)$. Since the criterion (3.1) is based on purely geometrical considerations, a word of warning is already in place. Light propagation between the element and target planes is in reality affected by diffraction, and hence the prescribed target distribution $S(u)$ can generally not be achieved exactly. This is true, in particular, if the spatial width of $S(u)$ is close to the diffraction limit [109].

Assuming that the incident field has a constant phase, the task of the element is to convert a normally incident ray at each point x into a ray that propagates at an angle θ given by

$$\tan\theta = \frac{u(x) - x}{\Delta z}. \tag{3.2}$$

The local ray direction is normal to the phase of the field just after the element, which is determined by the gradient of the phase function $\phi(x)$, and therefore we have (see, e.g., Ref. [107], Sect. 1.3.5)

$$\sin\theta = \frac{1}{k_0}\frac{\mathrm{d}\phi(x)}{\mathrm{d}x}, \tag{3.3}$$

where $k_0 = \omega_0/c = 2\pi/\lambda_0$. In paraxial approximation we can write $\tan\theta \approx \sin\theta \approx \theta$. Then, combining Eqs. (3.2) and (3.3) and integrating, we have

$$\phi(x) = \frac{k_0}{\Delta z}\int_0^x \left[u(x') - x'\right]\,\mathrm{d}x', \tag{3.4}$$

which provides the desired phase function of the element.

Let us consider the Gaussian to flat-top transformation [126,127] already illustrated in Fig. 3.1 as an example. The incident field is taken to have a Gaussian distribution

$$V(x) = \left(\frac{2}{\pi}\right)^{1/4} \exp\left(-\frac{x^2}{w^2}\right) \tag{3.5}$$

and hence the spatial distribution of its spectral density is given by

$$S(x) = \left(\frac{2}{\pi}\right)^{1/2} \exp\left(-\frac{2x^2}{w^2}\right). \tag{3.6}$$

The spectral density at the target plane is specified as

$$S(u) = \begin{cases} 1/2a & \text{if } |u| \leq a \\ 0 & \text{otherwise.} \end{cases} \tag{3.7}$$

The energy balance criterion (3.1) now gives a geometrical mapping criterion

$$u(x) = a \operatorname{erf}\left(\frac{\sqrt{2}x}{w}\right) \tag{3.8}$$

and the phase function given by Eq. (3.4) takes the form

$$\begin{aligned} \phi(x) = &-\frac{k_0 x^2}{2\Delta z} \\ &+ \frac{k_0 a}{\Delta z}\left\{\frac{w}{\sqrt{2\pi}}\left[\exp\left(-\frac{2x^2}{w^2}\right) - 1\right] + x \operatorname{erf}\left(\frac{\sqrt{2}x}{w}\right)\right\}. \end{aligned} \tag{3.9}$$

This is a superposition of a quadratic term and an aspheric term. The quadratic term represent the parabolic phase function of a thin lens [125] that would, in the absence of the aspheric term, focus light into a diffraction-limited Gaussian spot at the target plane. The aspheric term is responsible for creating aberrations that shape the spot into a flat-top form.

Instead of considering the Fresnel-domain beam shaping geometry of Fig. 3.1, one often wishes to shape the incident field into prescribed form in the far zone. In this case the coordinate u (and u') in Eq. (3.1) is interpreted as the x-component of the spatial-frequency vector and Eq. (3.4) is replaced by

$$\phi(x) = \int_0^x u(x')\,\mathrm{d}x'. \tag{3.10}$$

Let us assume that the incident field is still given by Eq. (3.5) and define the target distribution as

$$S(u) = \begin{cases} 1/2k_0\Phi & \text{if } |u| \leq a \\ 0 & \text{otherwise,} \end{cases} \tag{3.11}$$

where Φ represent the (paraxial) divergence half-angle of the flat-top profile (in radians). The mapping condition is now

$$u(x) = k_0\Phi \operatorname{erf}\left(\frac{\sqrt{2}x}{w}\right) \tag{3.12}$$

and, by inserting this into Eq. (3.10), we obtain the phase function

$$\phi(x) = k_0\Phi\left\{\frac{w}{\sqrt{2\pi}}\left[\exp\left(-\frac{2x^2}{w^2}\right) - 1\right] + x \operatorname{erf}\left(\frac{\sqrt{2}x}{w}\right)\right\}. \tag{3.13}$$

Because of the mapping into the far field, the quadratic focusing term is absent from this expression and only the aberration term remains.

3.2 REFRACTIVE CASE

Let us consider first the transformation of a polychromatic Gaussian field with frequency-invariant width w into a flat-top far-zone pattern with an angular half-width Φ using an optical element with an aspheric refractive surface profile (strictly speaking, for broadband fields, both w and Φ generally depend on frequency, but for a while we ignore this dependence for simplicity) The phase function at the design frequency ω_0 is given by Eq. (3.13) and the phase function at any other frequency ω has the form

$$\phi(x, \omega) = \frac{\omega}{\omega_0} D(\omega)\phi(x). \tag{3.14}$$

Here the term

$$D(\omega) = \frac{n(\omega) - 1}{n(\omega_0) - 1} \tag{3.15}$$

is a dispersion factor, where $n(\omega)$ is the frequency-dependent refractive index of the material used to realize the surface-relief profile. This dispersion factor can be ignored for quasimonochromatic light, but not for broadband light from thermal, RGB, femtosecond, or supercontinuum sources.

If we assume that the far-field diffraction pattern is observed in the back focal plane of an achromatic $2F$ Fourier-transforming system of focal length F and interpret u as a spatial coordinate in this target plane, the output field can be evaluated using the diffraction integral [125]

$$V(u,\omega) = \sqrt{\frac{\omega}{\mathrm{i}2\pi cF}} \int_{-\infty}^{\infty} V(x,\omega) \exp[\mathrm{i}\phi(x,\omega)] \exp\left(-\frac{\mathrm{i}\omega}{cF}ux\right) \mathrm{d}x, \tag{3.16}$$

where $V(x,\omega) = V(x)$ is given by Eq. (3.5) if the frequency dependence of w is ignored. If we assume that no beam-shaping element is in place and thus write $\phi(x,\omega) = 1$, the target-plane field at the design frequency is a diffraction-limited Gaussian spot with width

$$w_{\mathrm{F}} = \frac{2cF}{w\omega_0} = \frac{2F}{k_0 w} = \frac{F\lambda_0}{\pi w}. \tag{3.17}$$

Hence it is meaningful to define a 'times diffraction limit' expansion factor

$$Q = \frac{\Phi F}{w_{\mathrm{F}}} = \frac{w\omega_0}{2c}\Phi = \frac{1}{2}k_0 w\Phi = \frac{\pi w}{\lambda_0}\Phi. \tag{3.18}$$

The geometrical map-transform method can be expected to work well only if $Q \gg 1$.

If we also scale the x axis by introducing a normalized spatial variable $X = x/w$, Eq. (3.13) takes the form

$$\phi(X) = 2Q\left\{\frac{1}{\sqrt{2\pi}}\left[\exp\left(-2X^2\right) - 1\right] + X\,\mathrm{erf}\left(\sqrt{2}X\right)\right\}. \tag{3.19}$$

If we further define the normalized frequency $\Omega = \omega/\omega_0$ and the normalized Fourier-plane coordinate

$$U = \frac{u}{w_F} = \frac{w\omega_0}{2cT}u = \frac{k_0 w}{2F}u = \frac{\pi w}{F\lambda_0}u, \tag{3.20}$$

the dispersion term becomes

$$D(\Omega) = \frac{n(\Omega\omega_0) - 1}{n(\omega_0) - 1} \tag{3.21}$$

and the diffraction integral (3.16) is transformed into the form

$$V(U,\Omega) = C(\Omega) \int_{-\infty}^{\infty} \exp(-X^2) \times \exp\left[\mathrm{i}\Omega D(\Omega)\phi(X)\right] \exp\left(-\mathrm{i}2\Omega UX\right)\, \mathrm{d}X, \tag{3.22}$$

where $C(\Omega)$ is a factor that varies only slowly with Ω (see Paper II). This form is nice especially if dispersion is ignored, since then all quantities are dimensionless and do not depend on the design frequency ω_0.

So far we have assumed that w and Φ are independent on wavelength. However, broadband Gaussian pulses generated in spherical-mirror resonators are of isodiffracting type [71], i.e., the beam width $w(\omega)$ becomes frequency dependent but the so-called Rayleigh range $z_\mathrm{R} = \omega w^2(\omega)/2c$ is independent on frequency. Then we have the relation $w(\omega) = w/\sqrt{\Omega}$. In this case the input-field term $\exp(-X^2)$ in Eq. (3.22) is simply replaced with $\exp(-\Omega X^2)$.

3.3 DIFFRACTIVE CASE

3.3.1 Theory of generalized orders

Let us next consider, in general terms, the diffractive case, where the transmission function

$$t(x,\alpha) = \exp\left[\mathrm{i}\alpha\phi(x)\right] \tag{3.23}$$

is periodic with period $2\pi M$, M is a positive integer (called the harmonic parameter), α is a constant, and $\phi(x)$ is an arbitrary design phase function. Because of the periodicity, we may represent $t(x,\alpha)$ in the form of a generalized Fourier series [128]

$$t(x,\alpha) = \sum_{m=-\infty}^{\infty} G_m(\alpha) \exp\left[\mathrm{i}m\phi(x)/M\right] \tag{3.24}$$

where the Fourier coefficients are

$$G_m(\alpha) = \frac{1}{2\pi M}\int_0^{2\pi M} t(x,\alpha)\exp\left[-\mathrm{i}m\phi(x)/M\right]\,\mathrm{d}\phi(x)$$
$$= \frac{1}{2\pi M}\int_0^{2\pi M} \exp\left[\mathrm{i}\left(M\alpha - m\right)\phi(x)/M\right]\,\mathrm{d}\phi(x), \qquad (3.25)$$

and Eq. (3.23) was used to arrive at the latter form. Performing the integration and simplifying, we readily obtain

$$G_m(\alpha) = \mathrm{sinc}(M\alpha - m)\exp\left[\mathrm{i}\pi(M\alpha - m)\right], \qquad (3.26)$$

where $\mathrm{sinc}(x) = \sin(\pi x)/(\pi x)$. Since $G_m(0) = 1$, all light goes to order $m = M$ if $\alpha = 1$. For values of α around unity we have several generalized orders with $|G_m(\alpha)|$ significantly different from zero. These are located around order $m = M$ and they need to be included in the analysis. However, since the number of such orders is not large, the generalized-order expansion is numerically efficient.

3.3.2 Output field in diffractive case

Taking $\alpha = \Omega D(\Omega)$ in Eq. (3.26) and using the normalized spatial coordinate X, the complex-amplitude transmittance function of a harmonic diffractive element of harmonic order M can be represented in the form

$$t(X,\Omega) = \sum_{m=-\infty}^{\infty} G_m(\Omega)\exp\left[\mathrm{i}2\pi m\phi(X)/M\right], \qquad (3.27)$$

where

$$G_m(\Omega) = \mathrm{sinc}\left[M\Omega D(\Omega) - m\right]\exp\left\{\mathrm{i}\pi[M\Omega D(\Omega) - m]\right\}. \qquad (3.28)$$

We can now readily write a frequency-dependent expression corresponding to Eq. (3.22) for modulo $2\pi M$ elements in terms of generalized orders as

$$V(U,\Omega) = C(\Omega)\sum_{m=-\infty}^{\infty} G_m(\Omega)\int_{-\infty}^{\infty}\exp\left(-X^2\right)$$
$$\times\exp\left[\mathrm{i}m\phi(X)/M\right]\exp(-\mathrm{i}2\Omega UX)\,\mathrm{d}X. \qquad (3.29)$$

This allows us to study either purely diffractive elements (for which $M = 1$) or the transition from the diffractive to the refractive case (if we increase M). Again, for an isodiffracting incident wave, we just replace $\exp\left(-X^2\right)$ in Eq. (3.29) with $\exp\left(-\Omega X^2\right)$.

3.4 HYBRID CASE

The theory of generalized orders can also be applied to arbitrary hybrid refractive/diffractive structures, which are generalization of hybrid lenses [34, 35]. Let us expand the phase function given by Eq. (3.13) in a Taylor series:

$$\phi(X) = 2Q\sqrt{\frac{2}{\pi}}X^2 + \frac{2}{3}Q\sqrt{\frac{2}{\pi}}X^4 + \dots \tag{3.30}$$

The first term represents the phase function of a thin lens and the rest are aberration terms. We can therefore construct a hybrid element with phase function

$$\phi(X) = \phi_{\mathrm{R}}(X) + \phi_{\mathrm{D}}(X), \tag{3.31}$$

where

$$\phi_{\mathrm{R}}(X) = 2Qc\sqrt{\frac{2}{\pi}}X^2, \tag{3.32}$$

$$\phi_{\mathrm{D}}(X) = 2Q\left\{\frac{1}{\sqrt{2\pi}}\left[\exp\left(-2X^2\right) - 1\right] + X\,\mathrm{erf}\left(\sqrt{2}X\right) - c\sqrt{\frac{2}{\pi}}X^2\right\}, \tag{3.33}$$

and c is a constant. The phase function $\phi_{\mathrm{R}}(X)$ again represents a thin lens, which may be realized as a refractive element, and $\phi_{\mathrm{D}}(X)$ is an aberration term that can be realized as a modulo $2\pi M$ diffractive element with any desired harmonic parameter M. These two elements could be fabricated separately and put in contact.

Considering the field at any frequency, we have the refractive and diffractive phase functions

$$\phi_{\mathrm{R}}(X, \Omega) = \Omega D(\Omega)\phi_{\mathrm{R}}(X) \tag{3.34}$$

and

$$\phi_{\mathrm{D}}(X,\Omega) = \Omega D(\Omega)\phi_{\mathrm{D}}(X). \tag{3.35}$$

The diffraction formula from which the target-plane field can be obtained now reads as

$$\begin{aligned} V(U,\Omega) = C(\Omega)\int_{-\infty}^{\infty} &\exp\left(-X^2\right)\exp\left[\mathrm{i}\Omega D(\Omega)\phi_{\mathrm{R}}(X)\right] \\ &\times \exp\left(-\mathrm{i}2\Omega UX\right)\,\mathrm{d}X \\ + C(\Omega)\sum_{m=-\infty}^{\infty} G_m(\Omega)\int_{-\infty}^{\infty} &\exp\left(-X^2\right) \\ &\times \exp\left[\mathrm{i}m\phi_{\mathrm{D}}(X)/M\right]\exp\left(-\mathrm{i}2\Omega UX\right)\,\mathrm{d}X. \end{aligned} \tag{3.36}$$

Isodiffracting incident fields can be treated as in the previous cases.

3.5 EXAMPLES

Figure 3.2 illustrates the y-invariant $2F$ geometry considered to compare the performance of different types of beam shaping elements. In practice the distance between the beam shaping element and the lens is not critical (the element and the lens could even be in contact) as long as we are interested only in the intensity profile in the target plane and not the phase of the output field.

In this section we concentrate on spectrally integrated target-plane profiles

$$S(U) = \int_0^{\infty} S(U,\Omega)\mathrm{d}\Omega = \int_0^{\infty} S_0(\Omega)\left|V(U,\Omega)\right|^2\mathrm{d}\Omega, \tag{3.37}$$

where $S_0(\Omega)$ represents the spectral shape of the incident field. If this field is non-stationary, the frequency-integrated target-plane profile is directly proportional to the time-integrated intensity profile by as demonstrated in Appendix of Paper II. Hence the results to be presented apply both to stationary and non-stationary fields and are the same for both provided that $S_0(\Omega)$ is the same.

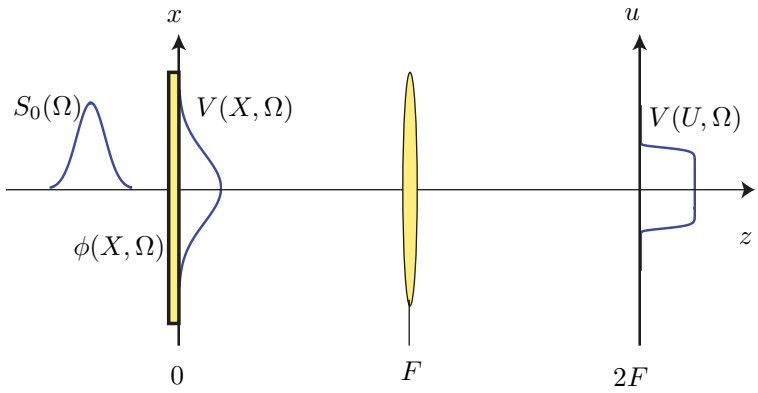

Figure 3.2: The 2F geometry for transformation of an incident field with spatial distribution $V(X,\Omega)$ and spectrum $S_0(\Omega)$ into a target field $V(U,\Omega)$ in the Fourier plane of an achromatic lens with focal length F, using a beam shaping element with phase function $\phi(X,\Omega)$ located at the plane $z = 0$.

Although any spectral profile $S_0(\omega)$ could be used, we assume specifically that the incident field has a Gaussian spectrum

$$S_0(\Omega) = S_0 \exp\left[-\frac{2\,(\Omega-1)^2}{\Omega_S^2}\right], \tag{3.38}$$

where Ω_S is the effective width of the spectrum normalized by the center wavelength ω_0. In the numerical examples we assume an isodiffracting Gaussian spatial profile of the form

$$V(X,\Omega) = \exp\left(-\Omega X^2\right). \tag{3.39}$$

Figure 3.3 shows the phase functions of refractive, diffractive and modulo $M = 5$ harmonic beam shaping elements for an expansion factor $Q = 20$. As we move from diffractive to hybrid and refractive cases, there are changes in phase jumps and phase height. These changes have significant effects in the target-plane profiles. Similarly, Fig 3.4 shows the phase functions of hybrid elements, where almost all the focusing power is contained in the refractive part if $c = 1$ and almost all the power is contained in the diffractive part when $c = 0.1$, and in the case $c = 0.6$, the focusing power is best

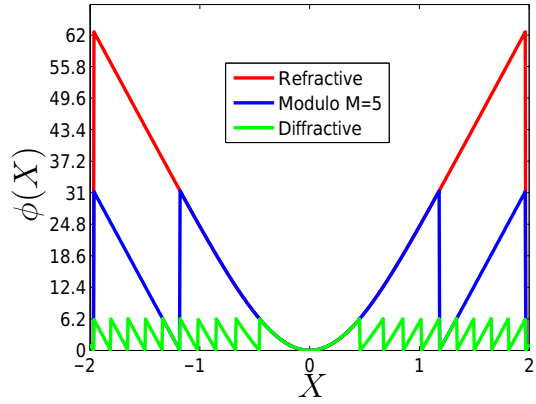

Figure 3.3: The design-frequency phase functions of purely refractive (red), purely diffractive (blue) and modulo $M = 5$ (green) beam shaping elements with $Q = 20$.

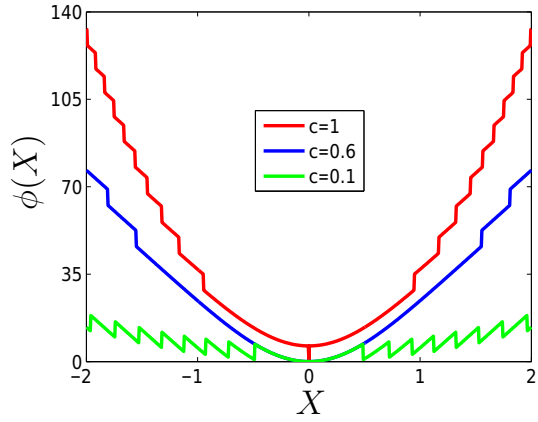

Figure 3.4: The design-frequency phase functions of a hybrid element when c=1 (red), c=0.6 (blue) and c=0.1 (green) with $Q = 20$.

contained in the refractive element in the sense that the diffractive element contains only few phase transitions.

Figure 3.5 shows how refractive, harmonic, and diffractive elements work for normalized wavelengths $\Lambda = 2\pi c/\Omega$ other than the design wavelength. Refractive elements work almost perfectly, as expected, for all the wavelengths considered. When we look at the diffractive and harmonic cases, there are strong fluctuations at wavelengths $\Lambda \neq 1$. If $\Lambda > 1$, profiles produced by a diffractive

element contain a central dip; if $\Lambda < 1$, one observes a central peak. These phenomena result from the zeroth generalized diffraction order being focused at the center of the Fourier-plane pattern as a narrow diffraction-limited spot that interferes with the contributions from other generalized orders. However, the frequency-integrated flat-top pattern is nearly as good as the one obtained with the refractive element. In the case of a harmonic element the central dip and peak disappear because the efficiency of the zeroth generalized order is low, as only a few orders around the main harmonic order $M = 5$ are significant. Again, the frequency-integrated flat-top profiles show good quality.

In the previous example the spectrum was relatively narrow. Let us next consider RGB illumination consisting of three discrete wavelengths $\lambda_R = 633$ nm (red), $\lambda_G = 532$ nm (green), and $\lambda_B = 473$ nm (blue). The corresponding frequencies are $\omega_R = 2.98 \times 10^{15}$ Hz, $\omega_G = 3.54 \times 10^{15}$ Hz, and $\omega_B = 3.99 \times 10^{15}$ Hz. The relative intensities of these sources are chosen as $S_R = 1$, $S_G = 0.6290$, and $S_B = 0.8177$ in order to produce white light in RGB space. The dispersion data are taken from Ref. [129] for polycarbonate.

Figure 3.6 illustrates the target profiles when no beam shaping element is placed in the setup, i.e., the diffraction-limited spots at the RGB wavelengths result in a frequency-integrated profile $S(U) = S_R(U) + S_G(U) + S_B(U)$. Figure 3.7 shows the individual profiles $S(U, \Lambda)$ generated by these sources when an element is present, as well as the resulting distributions $S(U)$.

Even though the spectrum in now non-symmetric and extends over most of the visible region, the standard diffractive element still works reasonably well if we consider only the frequency-integrated results shown by the black line. As expected, the individual profiles and the frequency-integrated result for the refractive element show an excellent flat-top profile also at individual wavelengths, but for the diffractive element the individual profiles at red and blue wavelengths are highly distorted. On the other hand, the modulo $M = 5$ hybrid element produces rather high-quality flat-top profiles at each wavelength. The individual profile widths are

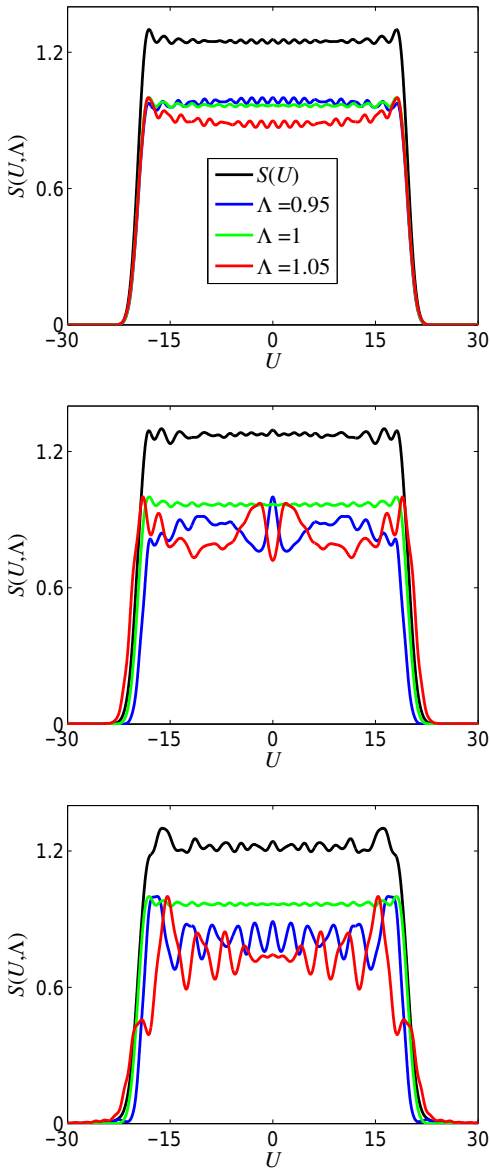

Figure 3.5: Fourier-plane spatial distributions $S(U, \Lambda)$ for (top) standard refractive, (center) standard diffractive, (bottom) modulo $M = 5$ diffractive elements.The black lines represent frequency-integrated profiles $S(U)$. Here the expansion factor is $Q = 20$.

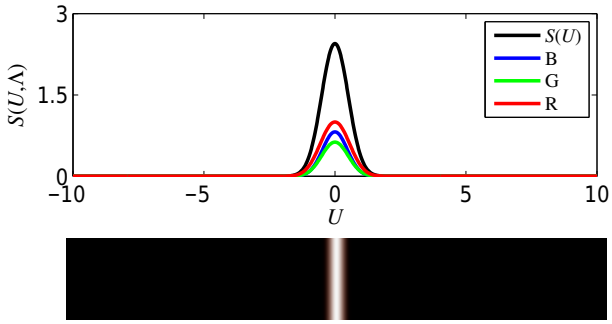

Figure 3.6: Target-plane profiles generated by red (R), green (G), and blue (B) light sources, and the frequency-integrated result with no element in place.

nearly the same. When we look at the true-color profiles as seen by human eye, those produced by the refractive and harmonic elements look bluish. In the case of a diffractive element there are significant color variations across the profile, with strongly red-colored edges. This is because the diffractive element spreads the pattern more at large wavelengths and the sign of dispersion is opposite to that of refractive elements. Figure 3.8 shows (as-yet unpublished) simulations on the hybrid case considered by means of the generalized-order theory in Sect 3.4. Here the individual profiles $S(U, \Lambda)$ generated by these sources when an element is present, as well as the resulting distributions $S(U)$ are shown. The combination of the refractive and diffractive powers at $c = 0.6$ leads to the best approximation for a flat-top profile.

3.6 SUMMARY

In summary, we can say that one can use refractive elements for all kinds of broadband applications. Diffractive elements also perform well for symmetric spectra that are some tens of nanometer wide. Such spectra are produced, e.g., by pulsed lasers or by superluminescent diodes. For highly broadband spectra (RGB or supercontinuum sources), diffractive elements perform satisfactorily if the color of the target profile is of no concern, and harmonic diffractive

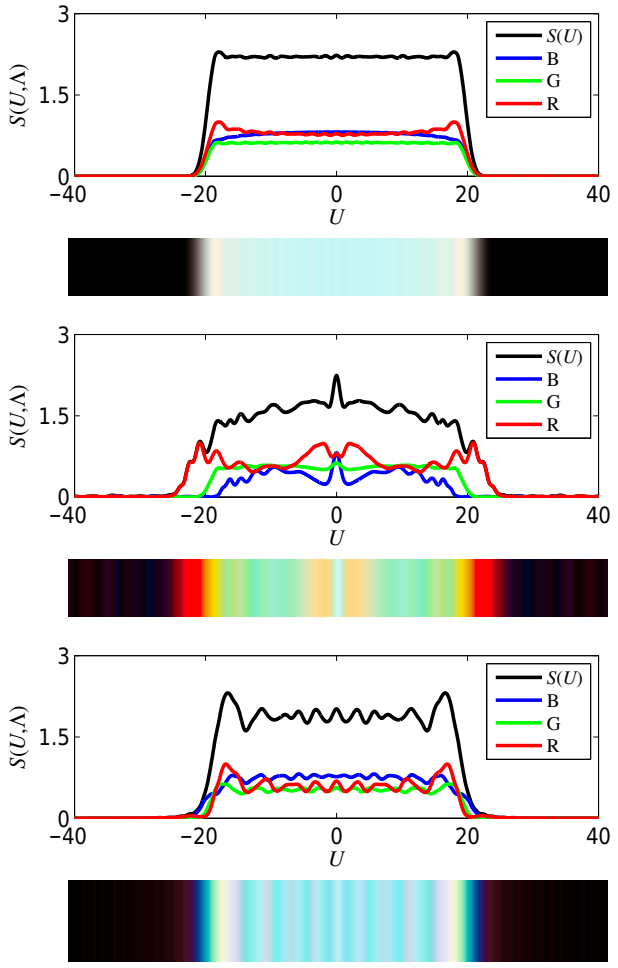

Figure 3.7: Target-plane profiles generated by red (R), green (G), and blue (B) light sources, and the frequency-integrated result for standard refractive (top), standard diffractive (center), and modulo $M = 5$ diffractive (bottom) elements. Also shown are true-color profiles as seen by the human eye.

elements produce quite acceptable results even in color-sensitive applications.

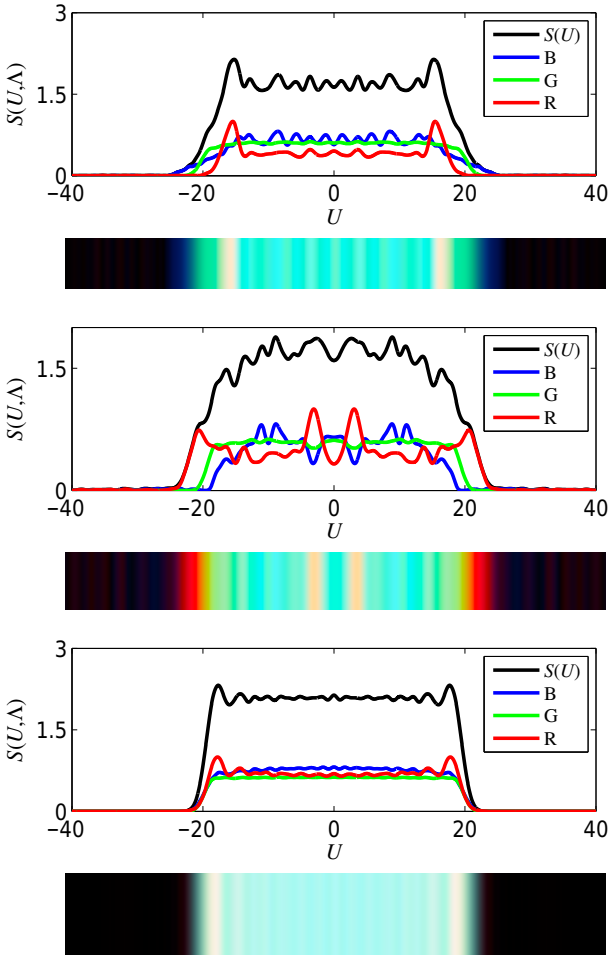

Figure 3.8: Target-plane profiles generated by red (R), green (G), and blue (B) light sources, and the frequency-integrated result for a hybrid element when $c = 1$ (top), $c = 0.1$ (center), and $c = 0.6$ (bottom). Also shown are true-color profiles as seen by the human eye.

4 Modal approaches to partial coherence

The propagation integrals of two-dimensionally varying fully coherent and monochromatic optical fields from one plane to another involve 2D integrals [125]. If the field is spatially partially coherent, 4D integrals need to be evaluated to connect the CSD functions at the two planes [1]. The evaluation of such integrals is a formidable numerical task, which is unmanageable because of computer-memory limitations alone if the field at the starting plane is of complicated shape. Fortunately there are ways around this difficulty: any stationary spatially partially coherent field has a rigorous space-frequency domain representation that takes the form of a superposition of fully coherent modal fields, which are solutions of a Fredholm integral equation of the second kind [48,49,130–132]. A corresponding modal representation applies also to non-stationary fields [133–135]. These representations, which are generally applicable to any partially coherent field, are introduced in Sect. 4.2.

Alternatively to the rigorous Mercer-type modal decompositions, one may in certain circumstances represent a spatially partially coherent field as a superposition of laterally displaced replicas of a single coherent field [51, 136–139]. Both of these approaches have been successfully used to model spatially partially coherent light [140] and, rather recently, to describe light radiated by certain realistic light sources [141–144]. Also this type of modal field representations, to be described in Sect 4.3, can be applied to represent the spectral and temporal coherence properties of non-stationary light [51].

4.1 PROPAGATION OF PARTIALLY COHERENT FIELDS

Suppose that we know the space-frequency-domain field distribution $V(\boldsymbol{\rho},\omega)$ at any transverse coordinate $\boldsymbol{\rho}=(x,y)$ across the plane $z=0$. The spatial-frequency content of the field is then determined by the angular spectrum [1]

$$A(\boldsymbol{\kappa},\omega)=\frac{1}{(2\pi)^2}\iint_{-\infty}^{\infty}V(\boldsymbol{\rho},\omega)\exp\left(-\mathrm{i}\boldsymbol{\kappa}\cdot\boldsymbol{\rho}\right)\,\mathrm{d}^2\rho, \tag{4.1}$$

where $\boldsymbol{\kappa}=\left(k_x,k_y\right)$ is the transverse component of the wave vector $\boldsymbol{k}=\left(k_x,k_y,k_z\right)$. The function $A(\boldsymbol{\kappa},\omega)$ also determines the field distribution in the far zone, i.e., when $z\to\infty$, and at any $\boldsymbol{r}=(\boldsymbol{\rho},z)$ with $z>0$ the field is given by

$$V(\boldsymbol{r},\omega)=\iint_{-\infty}^{\infty}A(\boldsymbol{\kappa},\omega)\exp\left(\mathrm{i}k_z z\right)\exp\left(\mathrm{i}\boldsymbol{\kappa}\cdot\boldsymbol{\rho}\right)\,\mathrm{d}^2\kappa, \tag{4.2}$$

where

$$k_z=\left(\omega^2/c^2-k_x^2-k_y^2\right)^{1/2}. \tag{4.3}$$

In the paraxial domain, where only field components at low spatial frequencies ($k_x^2+k_y^2\ll|\boldsymbol{k}|^2$) are significant, the Fresnel formula

$$V(\boldsymbol{r},\omega)=\frac{\omega}{\mathrm{i}2\pi cz}\exp\left(\mathrm{i}\omega z/c\right)\iint_{-\infty}^{\infty}V(\boldsymbol{\rho}',\omega)\left[\frac{\mathrm{i}\omega}{2cz}\left(\boldsymbol{\rho}-\boldsymbol{\rho}'\right)^2\right]\,\mathrm{d}^2\rho' \tag{4.4}$$

is applicable. The diffraction integrals Eq.(4.1)–(4.4) are two-dimensional and can be evaluated numerically in an efficient way using the Fast Fourier Transform (FFT) algorithm.

If the field at $z=0$ is known in the space-time domain, it is best to first move into the space-frequency domain using Eq. (2.3), propagate it in this domain, and finally move back to the space-time domain using Eq. (2.2).

The propagation integrals for the CSD of partially coherent light become four-dimensional. Considering, for example, non-stationary

fields and inserting from Eq. (4.4) into the definition (2.15) we have

$$W(\boldsymbol{r}_1,\boldsymbol{r}_2,\omega_1,\omega_2) = \iiiint_{-\infty}^{\infty} T(\boldsymbol{\kappa}_1,\boldsymbol{\kappa}_2,\omega_1,\omega_2)\exp\left[-\mathrm{i}\left(k_{z1}z_1 - k_{z2}z_2\right)\right] \times \exp\left[-\mathrm{i}\left(\boldsymbol{\kappa}_1\cdot\boldsymbol{\rho}_1 - \boldsymbol{\kappa}_2\cdot\boldsymbol{\rho}_2\right)\right]\,\mathrm{d}^2\kappa_1\,\mathrm{d}^2\kappa_2, \tag{4.5}$$

where

$$T(\boldsymbol{\kappa}_1,\boldsymbol{\kappa}_2,\omega_1,\omega_2) = \frac{1}{(2\pi)^4}\iiiint_{-\infty}^{\infty} W(\boldsymbol{\rho}_1,\boldsymbol{\rho}_2,\omega_1,\omega_2) \times \exp\left[\mathrm{i}\left(\boldsymbol{\kappa}_1\cdot\boldsymbol{\rho}_1 - \boldsymbol{\kappa}_2\cdot\boldsymbol{\rho}_2\right)\right]\,\mathrm{d}^2\rho_1\,\mathrm{d}^2\rho_2. \tag{4.6}$$

is known as the angular correlation function. This function defines the spatial-frequency content of the partially coherent field and also the field distribution in the far zone [1]. Four-dimensional propagation integrals are also obtained if stationary light is considered, and in the paraxial domain.

4.2 COHERENT-MODE REPRESENTATION

The decomposition of partially coherent fields into a complete set of fully coherent modes that are mutually uncorrelated has been known for a long time for stationary fields [48, 49, 130]. In this case we may always write the CSD at the plane $z = 0$ in the form of a Mercer representation

$$W(\boldsymbol{\rho}_1,\boldsymbol{\rho}_2,\omega) = \sum_{m=0}^{\infty}\alpha_m(\omega)\phi_m^*(\boldsymbol{\rho}_1,\omega)\phi_m(\boldsymbol{\rho}_2,\omega), \tag{4.7}$$

where the coefficients $\alpha_m(\omega)$ are real, non-negative eigenvalues that generally depend on ω. The functions $\phi_m(\boldsymbol{\rho},\omega)$ are the orthonormal eigenfunctions of the Fredholm integral equation of the second kind,

$$\iint_{-\infty}^{\infty} W(\boldsymbol{\rho}_1,\boldsymbol{\rho}_2,\omega)\phi_m(\boldsymbol{\rho}_1,\omega)\mathrm{d}\boldsymbol{\rho}_1 = \alpha_m(\omega)\phi_m(\boldsymbol{\rho}_2,\omega). \tag{4.8}$$

The functions $\phi_m(\boldsymbol{\rho},\omega)$ are the coherent modes associated with the CSD at $z = 0$. Since the summation in Eq. (4.7) is a linear combination of fully coherent contributions, it is possible to propagate

each individual coherent mode separately and then add these individual coherent modes to construct the propagated CSD in the form [136, 137]

$$W(\boldsymbol{r}_1, \boldsymbol{r}_2, \omega) = \sum_{m=0}^{\infty} \alpha_m(\omega) \phi_m^*(\boldsymbol{r}_1; \omega) \phi_m(\boldsymbol{r}_2; \omega),$$

where the relationship between the input-plane field $\phi_m(\boldsymbol{\rho}, \omega)$ and the field $\phi_m(\boldsymbol{r}, \omega)$ at any distance z can be determined using diffraction integrals for coherent light introduced above [1, 125].

The coherent-mode expansion for non-stationary fields [133–135] must deal with two frequencies. Thus we represent the two-frequency CSD at the plane $z = 0$ in the form

$$W(\boldsymbol{\rho}_1, \boldsymbol{\rho}_2, \omega_1, \omega_2) = \sum_{m=0}^{\infty} \alpha_m \phi_m^*(\boldsymbol{\rho}_1, \omega_1) \phi_m(\boldsymbol{\rho}_2, \omega_2), \tag{4.9}$$

the integral equation (4.8) is replaced by

$$\int_{-\infty}^{\infty} W(\boldsymbol{\rho}_1, \boldsymbol{\rho}_2, \omega_1, \omega_2) \phi_m(\boldsymbol{\rho}_1 \omega_1), \mathrm{d}\boldsymbol{\rho}_1 = \alpha_m \phi_m(\boldsymbol{\rho}_2, \omega_2).$$

and the propagated form of the coherent-mode expansion for non-stationary fields is

$$W(\boldsymbol{r}_1, \boldsymbol{r}_2, \omega_1, \omega_2) = \sum_{m=0}^{\infty} \alpha_m \phi_m^*(\boldsymbol{r}_1, \omega_1) \phi_m(\boldsymbol{r}_1, \omega_2). \tag{4.10}$$

It should be emphasized that, for non-stationary fields, the eigenvalues α_m no longer depend on frequency.

4.3 ELEMENTARY-FIELD REPRESENTATION

For a wide class of spatially partially coherent non-stationary fields, the CSD at the plane $z = 0$ may be written in the form of a superposition integral [51]

$$\begin{aligned} W(\boldsymbol{\rho}_1, \boldsymbol{\rho}_2, \omega_1, \omega_2) = \iint_{-\infty}^{\infty} & p(\bar{\boldsymbol{\rho}}, \omega_1, \omega_2) \\ & \times e^*(\boldsymbol{\rho}_1 - \bar{\boldsymbol{\rho}}, \omega_1) e(\boldsymbol{\rho}_2 - \bar{\boldsymbol{\rho}}, \omega_2) \, \mathrm{d}^2\bar{\rho} \end{aligned} \tag{4.11}$$

so that its spectral density is given by

$$S(\boldsymbol{\rho},\omega) = \iint_{-\infty}^{\infty} p(\bar{\boldsymbol{\rho}},\omega,\omega)\,|e(\boldsymbol{\rho}-\bar{\boldsymbol{\rho}},\omega)|^2\;\mathrm{d}^2\bar{\rho}. \tag{4.12}$$

Here $p(\bar{\boldsymbol{\rho}},\omega_1,\omega_2)$ is a real and non-negative function and the $e(\boldsymbol{\rho},\omega)$ is known as the elementary field associated with the CSD [138,145].

The field representation (4.13) expresses the CSD in the form of a weighted superposition of elementary fields of identical form, centered at laterally shifted positions $\bar{\boldsymbol{\rho}}$ in the plane $z = 0$. The elementary field can be propagated into any finite distance by methods given above for coherent fields, and the propagated CSD has the form

$$\begin{aligned} W(\boldsymbol{r}_1,\boldsymbol{r}_2,\omega_1,\omega_2) = \iint_{-\infty}^{\infty} & p(\bar{\boldsymbol{\rho}},\omega_1,\omega_2) \\ & \times e^*(\boldsymbol{r}_1-\bar{\boldsymbol{\rho}},\omega_1)e(\boldsymbol{r}_2-\bar{\boldsymbol{\rho}},\omega_2)\,\mathrm{d}^2\bar{\rho}. \end{aligned} \tag{4.13}$$

Now the 4D integrals needed to propagate partially coherent light have been reduced to evaluation of just one 2D integral. Once this is done, the result is used to construct the field at any distance simply by adding a weight distribution defined by $p(\bar{\boldsymbol{\rho}},\omega_1,\omega_2)$. Strictly analogous expressions may be readily written for stationary fields.

If we represent both the weight function and the elementary field in the form of a Fourier integrals

$$p(\bar{\boldsymbol{\rho}},\omega_1,\omega_2) = \iint_{-\infty}^{\infty} q(\boldsymbol{\kappa},\omega_1,\omega_2)\exp\left(i\boldsymbol{\kappa}\cdot\bar{\boldsymbol{\rho}}\right)\,\mathrm{d}^2\kappa \tag{4.14}$$

and

$$e(\boldsymbol{\rho},\omega) = \iint_{-\infty}^{\infty} f(\boldsymbol{\kappa},\omega)\exp\left(i\boldsymbol{\kappa}\cdot\boldsymbol{\rho}\right)\,\mathrm{d}^2\kappa, \tag{4.15}$$

a straightforward calculation shows that the angular correlation function defined in Eq. (4.6) takes the Schell-model form

$$T(\boldsymbol{\kappa}_1,\boldsymbol{\kappa}_2,\omega_1,\omega_2) = (2\pi)^2 f^*(\boldsymbol{\kappa}_1,\omega_1)f(\boldsymbol{\kappa}_2,\omega_2)q(\Delta\boldsymbol{\kappa},\omega_1,\omega_2), \tag{4.16}$$

where $\Delta\boldsymbol{\kappa} = \boldsymbol{\kappa}_2 - \boldsymbol{\kappa}_1$. If we now write the angular correlation function in the form

$$T(\boldsymbol{\kappa}_1,\boldsymbol{\kappa}_2,\omega_1,\omega_2) = \left[S(\boldsymbol{\kappa}_1,\omega_1)S(\boldsymbol{\kappa}_2,\omega_2)\right]^{1/2}\mu(\Delta\boldsymbol{\kappa},\omega_2,\omega_2), \tag{4.17}$$

the angular spectral density becomes

$$S(\boldsymbol{\kappa},\omega) = T(\boldsymbol{\kappa},\boldsymbol{\kappa},\omega,\omega) = (2\pi)^2 q(\mathbf{0},\omega,\omega)\,|f(\boldsymbol{\kappa},\omega)|^2 \tag{4.18}$$

and the complex degree of angular spectral coherence is

$$\begin{aligned}\mu(\Delta\boldsymbol{\kappa},\omega_1,\omega_2) = &\frac{q(\Delta\boldsymbol{\kappa},\omega_1,\omega_2)}{[q(\mathbf{0},\omega_1,\omega_1)q(\mathbf{0},\omega_2,\omega_2)]^{1/2}} \\ &\times \exp\left\{\mathrm{i}\left[\varphi(\boldsymbol{\kappa}_2,\omega_2) - \varphi(\boldsymbol{\kappa}_1,\omega_1)\right]\right\},\end{aligned} \tag{4.19}$$

where $\varphi(\boldsymbol{\kappa},\omega) = \arg[f(\boldsymbol{\kappa},\omega)]$. Hence the angular spectral density is fully determined by the elementary field at the plane $z = 0$ and the angular degree of spectral coherence is determined by the weight function of the elementary fields.

4.4 GAUSSIAN SCHELL MODEL SOURCES

Let us next consider a useful class of spatially partially coherent stationary fields for which the CSD is separable in x and y directions. Considering the x direction (with the understanding that the y direction can be treated in a strictly analogous way) and neglecting the ω dependence for brevity of notation, we write

$$W(x_1,x_2) = [S(x_1)S(x_2)]^{1/2}\,\mu(\Delta x) \tag{4.20}$$

with $\Delta x = x_2 - x_1$,

$$S(x) = S_0 \exp\left(-\frac{2x^2}{w^2}\right) \tag{4.21}$$

and

$$\mu(\Delta x) = \exp\left(-\frac{\Delta x^2}{2\sigma^2}\right). \tag{4.22}$$

This source is spatially of the Schell-model form, with Gaussian distributions of the spectral density and complex degree of spatial coherence characterized by parameters w and σ, and it is known as the Gaussian Schell-model (GSM) source [146]. This source is fully spatially coherent in the limit $\sigma \to \infty$, quasicoherent if $\sigma \approx w$, and

quasi-homogeneous if $\sigma \ll w$. Provided that $w \gg \lambda$ and $\sigma \gg \lambda$, the source radiates a directional, beamlike field characterized by Gaussian profiles of spectral density and complex degree of spatial coherence at all propagation distances [146–151].

The GSM source is one of the few spatially partially coherent sources for which the coherent-mode decomposition is known analytically [131, 136]. We have

$$W(x_1, x_2) = \sum_{m=0}^{\infty} \alpha_m \phi_m^*(x_1) \phi_m(x_2), \tag{4.23}$$

where the coherent modes are Hermite–Gaussian modes

$$\phi_m(x) = (2/\pi)^{1/4} \left(2^m m!\, w_\mathrm{c}\right)^{-1/2} H_m\left(\frac{\sqrt{2}x}{w_\mathrm{c}}\right) \exp\left(-\frac{x^2}{w_\mathrm{c}^2}\right), \tag{4.24}$$

where $H_m(x)$ is a Hermite polynomial of order m, and w_c is the transverse scale factor of the coherent modes. In order to obtain a Gaussian Schell-model source characterized by the parameters w and σ, we choose the modal scale factor as

$$w_\mathrm{c} = w\sqrt{\beta}, \tag{4.25}$$

where

$$\beta = \left[1 + (w/\sigma)^2\right]^{-1/2} \tag{4.26}$$

and assume that the modal weights obey the law

$$\alpha_m = S_0 \frac{\sqrt{2\pi} w}{1 + 1/\beta} \left(\frac{1-\beta}{1+\beta}\right)^m. \tag{4.27}$$

In addition to the Mercer coherent-mode representation, the GSM source also has an elementary-field representation [152, 153]. The weight function and the modal field are both of the Gaussian form, specifically

$$p(\bar{x}) = p_0 \exp\left(-\frac{2\bar{x}^2}{w_\mathrm{p}^2}\right) \tag{4.28}$$

and

$$e(x) = \exp\left(-\frac{x^2}{w_\mathrm{e}^2}\right) \tag{4.29}$$

with scale factors

$$w_{\mathrm{p}} = w\sqrt{1-\beta^2} \tag{4.30}$$

and

$$w_{\mathrm{e}} = w\beta, \tag{4.31}$$

where $p_0 = \sqrt{(2/\pi)\left(w_{\mathrm{p}}^{-2} + w_{\mathrm{e}}^{-2}\right)}$.

In paper I we have applied the modal representations to study the effect of partial coherence of light in beam shaping problems. In particular, we consider the Gaussian to flat-top transformation in the $2F$ geometry illustrated in Fig. 3.2, assuming that a Gaussian Schell-model field illuminates the beam shaping element. Figure 4.1 shows the Fourier-plane intensity profile using the Mercer-type coherent mode representation, where $\sigma = 0.2w$, $w = 1$ mm, $F = 100$ mm, and $\lambda = 633$ nm. When we look at individual coherent modes, we see that their target-plane intensity profiles do not look anything like flat-top profiles. The low-order modes have contributions to the center and as the order index increases, the main contribution shifts towards the edges. The incoherent superposition then gives a high-quality flat-top profile. In Figure 4.1, 14 modes were required to get a convergent result and a further increase in the number of modes did not affect the Fourier-plane profile significantly.

Figure 4.2 illustrates the Fourier-plane intensity profile obtained using the elementary field representation in a $4F$ setup considered in Paper I, with the beam shaping element located in the intermediate Fourier plane of the system. The target-plane profiles generated by individual elementary fields each have an approximately Gaussian spatially shifted shape but when we look at the summation of all elementary fields-field responses with appropriate weights, we get a good approximation of a flat-top profile. In this case 22 elementary fields were required to get a convergent result and further increase in the number of elementary fields did not affect the target-plane intensity profile significantly. Finally, in Figure 4.3 we show the effect of varying the ratio of σ/w in the flat-top profile. For a nearly coherent case we see the edge-enhancement effect ob-

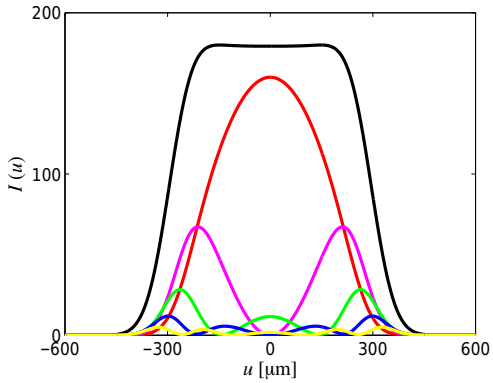

Figure 4.1: Fourier-plane intensity profiles generated by some lowest order Mercer modes of a Gaussian Schell-model field with $\sigma = 0.2w$, and the superposition of all significant modal contributions, which gives rise to a nearly flat-top intensity profile. The 0^{th} order (red), 1^{st} order (pink), 2^{nd} order (green), 3^{rd} order (blue) and 4^{th} order (yellow) show the individual mode contribution.

served already in Chapter 3, but the oscillations smooth out as the coherence decreases. However, then also the sidewalls become less steep.

4.4.1 Gaussian Schell model pulses

A Gaussian Schell-model plane-wave pulse train [154, 155] is characterized by a two-time CSD of the form

$$W(\omega_1, \omega_2) = [S(\omega_1)S(\omega_2)]^{1/2}\,\mu(\Delta\omega), \tag{4.32}$$

where $\Delta\omega = \omega_2 - \omega_1$. The spectral density is given by

$$S(\omega) = S_0 \exp\left[-\frac{2}{\Omega^2}\,(\omega - \omega_0)^2\right], \tag{4.33}$$

and the complex degree of spectral coherence is

$$\mu(\Delta\omega) = \exp\left(-\frac{\Delta\omega^2}{2\Omega_\mu^2}\right), \tag{4.34}$$

where Ω is the characteristic width of the spectrum, Ω_μ is the spectral coherence width, and ω_0 is the central frequency of the spectrum. When $\Omega_\mu/\Omega \to \infty$, we obtain a fully spectrally coherent

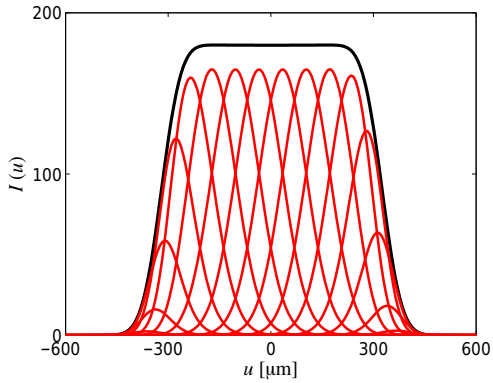

Figure 4.2: Fourier-plane intensity profiles generated by some laterally displaced elementary field modes when $\sigma = 0.2w$. The red lines are individual elementary-field contributions.

pulse train, and when $\Omega_\mu/\Omega \ll 1$ one can talk about a quasi-stationary train of pulses.

In analogy with spatial GSM sources, the GSM pulse train has both a coherent-mode representation and an elementary-field decomposition. The coherent mode-decomposition takes the form of a superposition of spectral Hermite–Gaussian modes: we have

$$W(\omega_1, \omega_2) = \sum_{m=0}^{\infty} \alpha_m \phi_m^*(\omega_1) \phi_m(\omega_2), \tag{4.35}$$

where

$$\phi_m(\omega) = (2/\pi)^{1/4} \left(2^m m!\, \Omega_c\right)^{-1/2} H_m\left[\frac{\sqrt{2}\,(\omega - \omega_0)}{\Omega_c}\right] \times \exp\left[-\frac{(\omega - \omega_0)^2}{\Omega_c^2}\right]. \tag{4.36}$$

The characteristic spectral width of the coherent modes is

$$\Omega_c = \Omega\sqrt{\beta}, \tag{4.37}$$

where the spectral β parameter is defined as

$$\beta = \left[1 + \left(\Omega/\Omega_\mu\right)^2\right]^{-1/2} \tag{4.38}$$

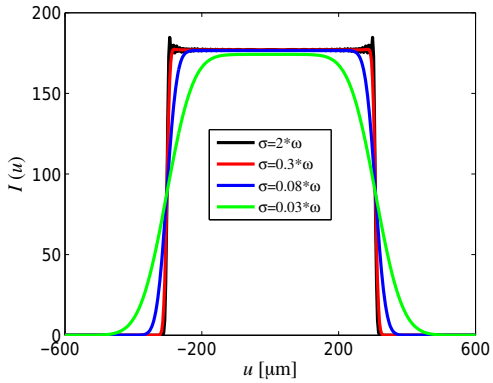

Figure 4.3: Effect of varying the degree of spatial coherence in the shape of the flat-top profile.

and the expansion coefficients are chosen as

$$\alpha_m = S_0 \frac{\sqrt{2\pi}\Omega}{1+1/\beta} \left(\frac{1-\beta}{1+\beta}\right)^m \tag{4.39}$$

in analogy with Eq. (4.27) in the spatial domain.

Let us now consider a general linear optical system illustrated in Fig. 4.4, which is described by a response function $K(u,x,\omega)$ such that a coherent incident field $V_0(x,\omega)$ in the input plane is transformed into a field

$$V(u,\omega) = \int_{-\infty}^{\infty} t(x,\omega) V_0(x,\omega) K(u,x,\omega) \mathrm{d}x. \tag{4.40}$$

in the output plane (we still consider the y-invariant case). Here $t(x,\omega)$ represents the complex-amplitude transmittance function of an optical element (such as a beam shaping element) placed in the input plane. If the incident field is spectrally stochastic, it may be written in the form $U_0(x,\omega) = a(\omega)V_0(x,\omega)$, where $a(\omega)$ is a random function with spectral two-frequency CSD

$$W(\omega_1,\omega_2) = \langle a^*(\omega_1) a(\omega_2) \rangle, \tag{4.41}$$

which we assume to obey the Gaussian Schell model. The space-frequency domain CSD of the incident field, which we assume to

be fully spatially coherent in the spectral domain, may be written as [68]

$$W_0(x_1, x_2, \omega_1, \omega_2) = W(\omega_1, \omega_2) V_0^*(x_1, \omega_1) V_0(x_2, \omega_2) \tag{4.42}$$

and the field at the output plane of the system takes the form

$$W(u_1, u_2, \omega_1, \omega_2) = W(\omega_1, \omega_2) V^*(u_1, \omega_1) V(u_2, \omega_2). \tag{4.43}$$

We further assume, as in Paper III, that the spatial field profile of the incident field represents the waist of the fundamental isodiffracting Gaussian mode of a spherical-mirror resonator [156], i.e.,

$$V_0(x; \omega) = V_0 \exp\left(-\frac{\omega}{\omega_0} \frac{x^2}{w^2}\right), \tag{4.44}$$

where w characterizes the beam width at $\omega = \omega_0$. In what follows, we also assume that the field just defined is incident on Gaussian to flat-top beam shaping elements discussed in Chapter 3, and that the optical system is simply a section of free space so that

$$K(u, x, \omega) = \sqrt{\frac{\omega}{\mathrm{i}2\pi cz}} \exp\left(\mathrm{i}\omega z/c\right) \exp\left[\frac{\mathrm{i}\omega}{2cz} (u - x)^2\right] \tag{4.45}$$

is the Fresnel transform kernel for propagation over a distance z.

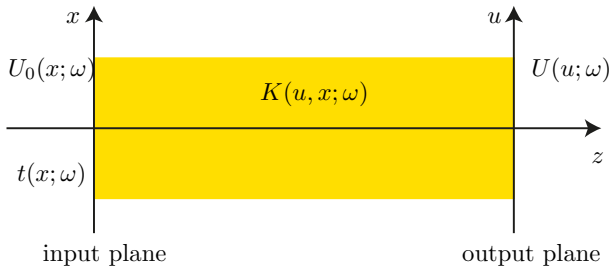

Figure 4.4: The beam shaping geometry, where x and u denote the transverse coordinates in the input and output planes, separated by an optical system with a response function $K(u, x, \omega)$. A thin beam-shaping element with complex-amplitude transmission function $t(x, \omega)$ transforms the incident field $U_0(x, \omega)$ into a spatially shaped output field $U(u, \omega)$.

If we express the spectral CSD $W(\omega_1, \omega_2)$ in the form of a coherent-mode representation, the target-plane spatiotemporal CSD given by

Eq. (4.43) may be rewritten in the form

$$W(u_1, u_2; \omega_1, \omega_2) = \sum_{m=0}^{\infty} \alpha_m \phi_m^*(\omega_1) \phi_m(\omega_2) V^*(u_1; \omega_1) V(u_2; \omega_2). \tag{4.46}$$

The spatiotemporal properties of the target-plane field are characterized by the two-time MCF, which is obtained by applying the generalized Wiener–Khintchine theorem for non-stationary light, which according to Eq. (2.20) now reads as

$$\Gamma(u_1, u_2, t_1, t_2) = \iint_0^{\infty} W(u_1, u_2, \omega_1, \omega_2) \times \exp\left[\mathrm{i}\left(\omega_1 t_1 - \omega_2 t_2\right)\right] \mathrm{d}\omega_1 \, \mathrm{d}\omega_2. \tag{4.47}$$

On inserting from Eq. (4.46) into Eq. (4.47) we have

$$\Gamma(u_1, u_2; t_1, t_2) = \sum_{m=0}^{\infty} \alpha_m V_m^*(u_1; t_1) V_m(u_2; t_2), \tag{4.48}$$

where

$$V_m(u; t) = \int_0^{\infty} \phi_m(\omega) V(u; \omega) \exp\left(-\mathrm{i}\omega t\right) \mathrm{d}\omega. \tag{4.49}$$

Hence the space-time intensity profile in the target plane is

$$I(u; t) = \sum_{m=0}^{\infty} \alpha_m \left| V_m(u; t) \right|^2. \tag{4.50}$$

We proceed to present some examples of these intensity profiles, noting that Eq. (4.48) would also allow us to study the time-domain spatial coherence in the target plane by examining the function $\Gamma(u_1, u_2; t, t)$, or the spatial variations of the two-time temporal coherence by studying the function $\Gamma(u, u; t_1, t_2)$.

Figure 4.5 illustrates the space-frequency and space-time profiles of Gaussian Schell-model pulse trains in the target plane of a refractive beam shaping element. The following set of parameters is assumed. The central wavelength of the pulse train is $\lambda_0 = 800$ nm (i.e., $\omega_0 \approx 2.36 \times 10^{15}$ Hz), the propagation distance

is $z = 0.5$ m, the incident beam diameter at the central wavelength is $w = 0.3$ mm, and the spectral width of the incident pulse train is $\Omega = 6 \times 10^{13}$ Hz, which implies an axial temporal half-width of $T = 2/\Omega \approx 33$ fs in the fully coherent case. The super-Gaussian parameter of the beam shaping element is $Q = 20$ as in Chapter 3, which implies a target spot half-width $w \approx 4.2$ mm, ensuring that we are well within the paraxial domain. The space-frequency profile in the target plane is shown on top of Fig. 4.5, while the bottom row displays space-time intensity profiles for different values of the ratio Ω_μ/Ω, revealing the effects of partial spectral coherence in the spatiotemporal profiles.

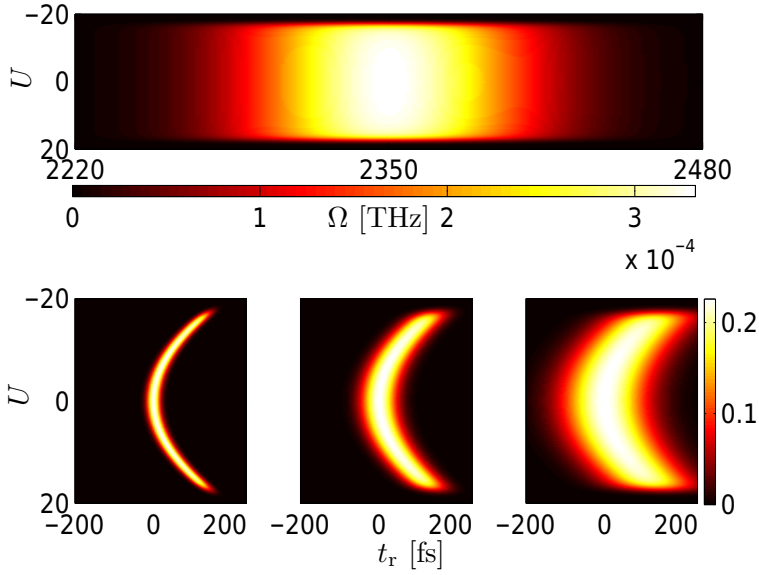

Figure 4.5: Top: Target-plane space-frequency profile for a Gaussian Schell-model pulse train. Bottom: Space-time profiles of pulse trains with the same spectral width but different spectral coherence widths $\Omega_\mu/\Omega = 3$ (left), $\Omega_\mu/\Omega = 0.5$ (center), and $\Omega_\mu/\Omega = 0.2$ (right). The horizontal axis in the bottom-row figures represents the retarded time $t_\mathrm{r} = t - z/c$.

Figure 4.5 shows that good-quality space-frequency-domain flat-top profiles are obtained throughout the entire spectral extent of the pulse train. However, the space-time intensity distributions are

bent. This implies that the axial part of each pulse is seen first at the target plane. In fact, the on-axis pulse passes the target plane before any significant contributions arrive at the edges of the flat-top profile. Reduction of the spectral coherence implies a widening of the temporal profile throughout the flat-top region, as one would expect since also the temporal width of the incident pulse increases when the degree of spectral coherence is reduced. Figure 4.6 shows the temporal bending of the profile as the pulse propagates.

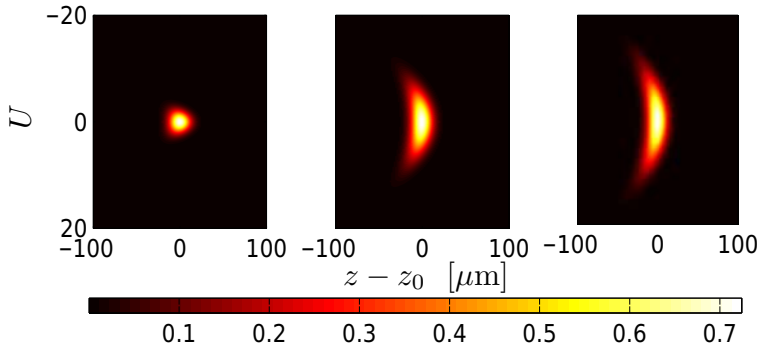

Figure 4.6: Spatial intensity profiles of a pulse train with $Q = 20$ and $\Sigma/\Omega = 0.5$ when the central maximum of the pulse is at $z = 0.1$ m (left), $z = 0.3$ m (center), and $z = 0.5$ m (right).

4.4.2 Supercontinuum pulse trains

Supercontinuum (SC) pulses were first observed by Alfano and Shapiro [157]. These spectrally broadband light pulses have gained many applications, for example in imaging, bio-medicine [158–160], metrology [161], and telecommunication [162]. We can represent SC pulse trains using the Mercer coherent-mode representation [163], by first constructing the CSD or MCF using numerically simulated pulse realizations generated in microstructured fibers [95, 164] and then solving the coherent modes $\phi_m(\omega)$ and their weights α_m numerically from the Fredholm equation. Alternatively, we can use the elementary field representation to describe SC pulse trains in an approximate way [165] . In the examples considered below, we

make direct use of numerically simulated field realizations $E_n(\omega)$ and write the spectral CSD in the form

$$W(\omega_1, \omega_2) = \langle E^*(\omega_1) E(\omega_2) \rangle = \frac{1}{N} \sum_{n=1}^{N} E_n^*(\omega_1) E_n(\omega_2). \tag{4.51}$$

The space-time field realizations in the target plane are of the form

$$V_n(u, t) = \int_0^\infty E_n(\omega) V(u, \omega) \exp(-\mathrm{i}\omega t)\, \mathrm{d}\omega. \tag{4.52}$$

where $V(u; \omega)$ is the spatial target-plane field distribution. Hence the space-time intensity distribution in the target plane is obtained as an ensemble average

$$I(u, t) = \langle |V(u, t)|^2 \rangle = \frac{1}{N} \sum_{n=1}^{N} |V_n(u, t)|^2 . \tag{4.53}$$

Figure 4.7 shows the mean spectral density and the mean temporal intensity of an SC pulse train and their decompositions into quasi-stationary (qs) and quasi-coherent (qc) parts [93, 94]. We can see many fluctuations in the qc spectral density and a much smoother qs profile. The temporal intensity profile also fluctuates rapidly, showing several spikes within a time scale of a few picoseconds. Figure 4.9 illustrates the space-frequency and space-time profiles at the target plane of a refractive beam shaping element: here we assume geometrical parameters $w = 0.3$ mm, $z = 0.5$ m, and $Q = 10$. Even though there are fluctuations in the spectral density, the space-frequency profile is a good approximation of a flat-top profile. The spatio-temporal profile shows bending similar to that seen in the case of GSM pulses, but the bending is comparatively smaller since the SC pulses considered here are in the picosecond time scale, while femtosecond GSM pulses were considered.

4.5 SUMMARY

To summarize the results presented in this chapter, we have considered representations of partially coherent fields in the form of

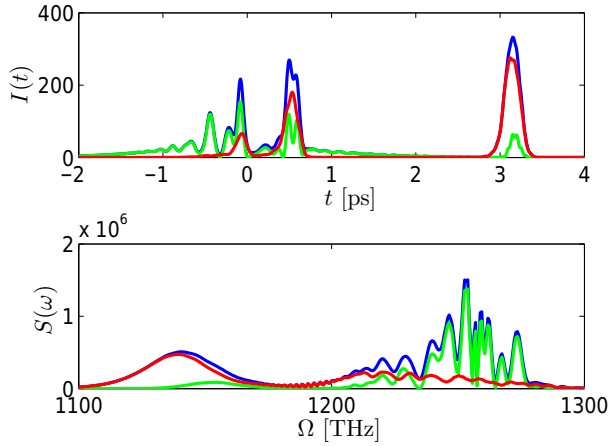

Figure 4.7: The temporal intensity (top) and the spectral density (bottom) of the incident SC pulse train. The blue lines represent the entire pulse train, whereas the green and red lines illustrate the quasi-coherent (qc) and quasi-stationary (qs) contributions, respectively.

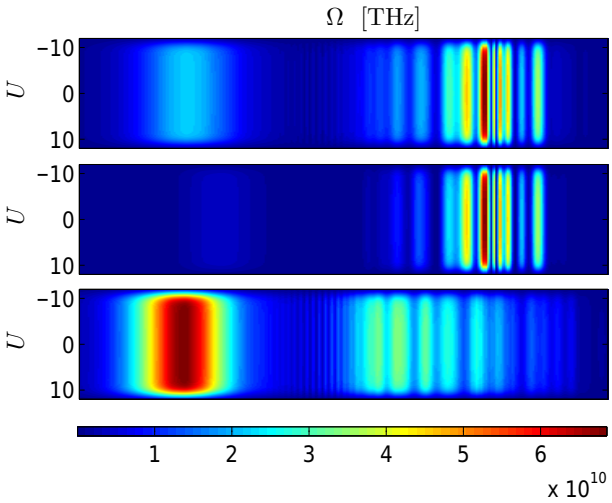

Figure 4.8: The target-plane space-frequency profiles produced by the SC pulse train considered in Fig. 4.7. Top: the entire pulse train. Middle: the qc contribution. Bottom: the qs contribution. The profiles are scaled to their maximum values in each case.

coherent-mode superpositions and shown how such representations help to reduce the computational complexity of propagation problems. The results were applied to shaping spatially partially

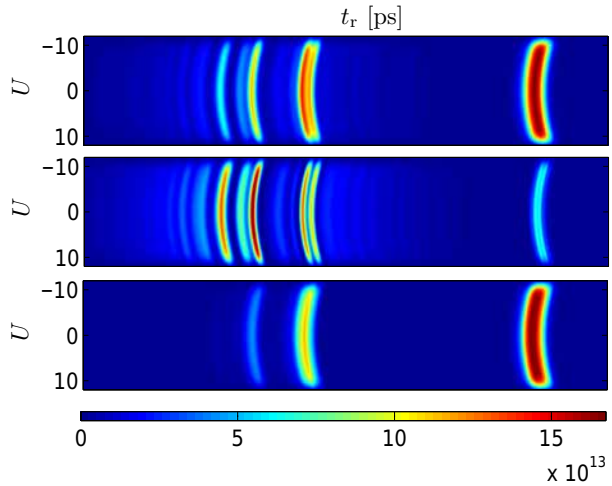

Figure 4.9: (a) The target-plane space-time profiles produced by the SC pulse train considered in Fig. 4.7. Top: the entire pulse train. Middle: the qc contribution. Bottom: the qs contribution.The profiles are scaled to their maximum values in each case.

coherent stationary light and spectrally partially coherent pulse trains. In the case of spatial beam shaping, the profiles generated by individual modes were seen to have widely different target-plane properties, but the modal superpositions were found to produce good approximations of the desired flat-top profiles. In the case of ultrashort pulse trains, high-quality target profiles were observed at each individual frequency. The spatio-temporal target-plane profiles were found to bend such that the arrival times of the pulses at the target plane depend on the lateral position.

5 Partially coherent imaging

We saw in Sect. 4.1 that propagating partially coherent fields in free space requires the evaluation of 4D integrals if the cross-spectral density function is considered directly. The same is generally true if we consider imaging problems with partially coherent light, assuming that the field incident on an object is described by a CSD of arbitrary form [166–168]. Often one can assume that the incident field is generated with a primary incoherent source placed in the front focal plane of a 2F Fourier-transform system (condenser), with the object located in the back focal plane. Then the CSD takes a specific (Schell-model) form, which depends only on coordinate differences. Numerous methods have been developed to approach this type of partially coherent imagery problems [169–177]. However, these methods are not applicable in all circumstances.

The computational complexity of free-space propagation and beam shaping problems can be reduced dramatically if modal methods are used, as we saw in Chapt. 4. It is therefore natural to apply them also to imaging problems. Some steps in this direction have been taken using the Mercer coherent-mode method [178–180], and the use of the elementary-field representation has also been suggested [52]. In this chapter we formulate the imaging problem using both of these modal approaches to model the partially coherent field incident on an object described by a complex-amplitude transmission function of arbitrary form. We compare them in the case of imaging of a slit. We then concentrate on the elementary-field approach, considering imaging by a telecentric system. The coherent system response to each laterally shifted elementary field mode is evaluated separately and the final image is evaluated by summing these contributions incoherently. We stress that this method is not only applicable to fields generated by an incoherent source in a condenser system, but to all cases where the incident field has an elementary-field representation (so that its angular correlation

function is of the Schell-model form). Numerical examples are presented on a 2D object displaying the characters UEF; more examples can be found in Paper IV.

5.1 IMAGING WITH COHERENT LIGHT

The general imaging geometry to be considered is illustrated in Fig. (5.1). The spatial coordinates at the object plane O are denoted by (x', y'), those at the intermediate Fourier plane A by (k_x, k_y), and those at the image plane I by (x, y). The object is described by a complex-amplitude transmittance function $t(x', y')$ and the pupil at A by a transmission function $P(k_x, k_y)$. The pupil function may be complex-valued in order to describe systems with aberrations or, as in Paper I, beam shaping elements. In the latter case we assume that $t(x', y') = 1$, i.e., no object is present in the system.

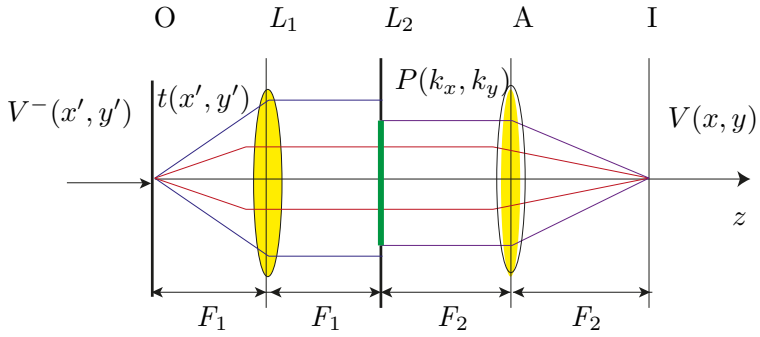

Figure 5.1: Imaging of an object at plane O by a telecentric system consisting of lenses L_1 and L_2 (focal lengths F_1 and F_2) through a pupil in the intermediate Fourier plane A.

Considering first coherent illumination of the object by a field $V^-(x', y')$, where the explicit frequency dependence is suppressed for brevity of notation, the field transmitted by the object is

$$V(x', y') = t(x', y')V^-(x', y'). \tag{5.1}$$

The field incident on the pupil plane is essentially the spatial Fourier

transform of $V(x', y')$ and may be expressed in the form [125]

$$V^-(k_x, k_y) = \frac{\omega}{\mathrm{i}2\pi c F_1} \iint_{-\infty}^{\infty} V(x', y') \times \exp\left[-\frac{\mathrm{i}\omega}{cF_1}\left(k_x x' + k_y y'\right)\right] \mathrm{d}x'\,\mathrm{d}y'. \tag{5.2}$$

After passage through the pupil, we then have

$$V(k_x, k_y) = P(k_x, k_y) V^-(k_x, k_y) \tag{5.3}$$

and finally the field in the image plane is

$$V(x, y) = \frac{\omega}{\mathrm{i}2\pi c F_2} \iint_{-\infty}^{\infty} V(k_x, k_y) \times \exp\left[-\frac{\mathrm{i}\omega}{cF_2}\left(k_x x + k_y y\right)\right] \mathrm{d}k_x\,\mathrm{d}k_y. \tag{5.4}$$

Hence the computation of the image field requires two 2D Fourier transforms, which can again be easily computed using the FFT algorithm.

The Fourier-transform nature of Eqs. (5.2) and (5.4) becomes even more apparent if we introduce normalized object-plane and image-plane coordinates

$$\tilde{x}' = \frac{\omega}{cF_1} x', \quad \tilde{y}' = \frac{\omega}{cF_1} y', \quad \tilde{x} = -\frac{\omega}{cF_2} x, \quad \tilde{y} = -\frac{\omega}{cF_2} y. \tag{5.5}$$

The magnification of the system, generally defined as $M = x'/x = y'/y$, is equal to $M = -F_2/F_1$ for the system in Fig. (5.1). Hence the normalized coordinates provide a convenient 1:1 mapping $(\tilde{x}, \tilde{y}) \leftrightarrow (\tilde{x}', \tilde{y}')$ between the object and image planes. The propagation formula (5.2) in these modified coordinates reads as

$$V^-(k_x, k_y) = \frac{cF}{\mathrm{i}2\pi\omega} \iint_{-\infty}^{\infty} V(\tilde{x}', \tilde{y}') \exp\left[-\mathrm{i}\left(k_x \tilde{x}' + k_y \tilde{y}'\right)\right] \mathrm{d}\tilde{x}'\,\mathrm{d}\tilde{y}', \tag{5.6}$$

which (apart from the factor in front) represents a direct Fourier transform, and Eq. (5.4) takes the form

$$V(\tilde{x}, \tilde{y}) = \frac{\omega}{\mathrm{i}2\pi c F_2} \iint_{-\infty}^{\infty} V(k_x, k_y) \exp\left[\mathrm{i}\left(k_x \tilde{x} + k_y \tilde{y}\right)\right] \mathrm{d}k_x\,\mathrm{d}k_y \tag{5.7}$$

of an inverse Fourier transform. If we now insert Eqs. (5.3) and (5.6) into Eq. (5.7), we arrive at a linear superposition integral

$$V(\tilde{x},\tilde{y}) = \iint_{-\infty}^{\infty} V(\tilde{x}',\tilde{y}')K(\tilde{x}-\tilde{x}',\tilde{y}-\tilde{y}')\,\mathrm{d}\tilde{x}'\,\mathrm{d}\tilde{y}', \tag{5.8}$$

where

$$K(x,y) = \frac{1}{(2\pi)^2 M}\iint_{-\infty}^{\infty} P(k_x,k_y)\exp\left[\mathrm{i}\left(k_x x + k_y x\right)\right]\,\mathrm{d}k_x\,\mathrm{d}k_y \tag{5.9}$$

is known as the impulse response (or point spread function) of the system.

5.2 IMAGING WITH PARTIALLY COHERENT LIGHT

In the spatially partially coherent case, the CSD at the output plane is obtained by inserting Eq. (5.8) into the definition

$$W(\tilde{x}_1,\tilde{y}_1,\tilde{x}_2,\tilde{y}_2) = \langle V^*(\tilde{x}_1,\tilde{y}_1)V(\tilde{x}_2,\tilde{y}_2)\rangle, \tag{5.10}$$

This immediately gives the result

$$\begin{aligned} W(\tilde{x}_1,\tilde{y}_1,\tilde{x}_2,\tilde{y}_2) = {} & \iiiint_{-\infty}^{\infty} W(\tilde{x}_1',\tilde{y}_1',\tilde{x}_2',\tilde{y}_2')K^*(\tilde{x}_1-\tilde{x}_1',\tilde{y}_1-\tilde{y}_1') \\ & \times K(\tilde{x}_2-\tilde{x}_2',\tilde{y}_2-\tilde{y}_2')\,\mathrm{d}\tilde{x}_1'\,\mathrm{d}\tilde{y}_1'\,\mathrm{d}\tilde{x}_2'\,\mathrm{d}\tilde{y}_2', \end{aligned} \tag{5.11}$$

which is a nonlinear 4D superposition integral.

Alternatively to using this result directly, we may first evaluate the CSD incident on A by

$$\begin{aligned} W^-(k_{x1},k_{y1},k_{x2},k_{y2}) = {} & -\left(\frac{cF_1}{2\pi\omega}\right)^2 \iiiint_{-\infty}^{\infty} W(\tilde{x}_1',\tilde{y}_1',\tilde{x}_2',\tilde{y}_2') \\ & \times \exp\left[\mathrm{i}\left(k_{x1}\tilde{x}_1' + k_{y1}\tilde{y}_1' - k_{x2}\tilde{x}_2' - k_{y2}\tilde{y}_2'\right)\right]\,\mathrm{d}\tilde{x}_1'\,\mathrm{d}\tilde{y}_1'\,\mathrm{d}\tilde{x}_2'\,\mathrm{d}\tilde{y}_2', \end{aligned} \tag{5.12}$$

then calculate the field transmitted by the pupil by

$$W(k_{x1},k_{y1},k_{x2},k_{y2}) = P^*(k_{x1},k_{y1})P(k_{x2},k_{y2})W^-(k_{x1},k_{y1},k_{x2},k_{y2}), \tag{5.13}$$

and finally determine the image-plane field from

$$W(\tilde{x}_1,\tilde{y}_1,\tilde{x}_2,\tilde{y}_2) = -\left(\frac{\omega}{2\pi c F_2}\right)^2 \iiint_{-\infty}^{\infty} W(k_{x1},k_{y1},k_{x2},k_{y2}) \times \exp\left[-\mathrm{i}\left(k_{x1}\tilde{x}_1' + k_{y1}\tilde{y}_1' - k_{x2}\tilde{x}_2' - k_{y2}\tilde{y}_2'\right)\right] \mathrm{d}k_{x1}\,\mathrm{d}k_{y1}\,\mathrm{d}k_{x2}\,\mathrm{d}k_{y2}. \tag{5.14}$$

However, this procedure also involves 4D integrals which need to be reduced to 2D form to allow numerically efficient evaluation [181–184], a task in which we will next concentrate.

5.2.1 Mercer coherent mode representation

Let us denote the coherent modes of the incident field by $\varphi_n(\tilde{x}',\tilde{y}')$. After transmission through the object we then have

$$\phi_m(\tilde{x}',\tilde{y}') = t(\tilde{x}',\tilde{y}')\varphi_m(\tilde{x}',\tilde{y}'). \tag{5.15}$$

The modal contributions to the image-plane CSD are denoted by $\phi_m(\tilde{x},\tilde{y})$. We may now expand the CSD of the incident field in the form of a coherent-mode series

$$W^-(\tilde{x}_1',\tilde{y}_1',\tilde{x}_2',\tilde{y}_2') = \sum_{m=0}^{M} \alpha_m \varphi_m^*(\tilde{x}_1',\tilde{y}_1')\varphi_m(\tilde{x}_2',\tilde{y}_2'). \tag{5.16}$$

If we define a coherent-mode response of the system as

$$\phi_m(\tilde{x},\tilde{y}) = \iint_{-\infty}^{\infty} \phi_m(\tilde{x}',\tilde{y}')K(\tilde{x}-\tilde{x}',\tilde{y}-\tilde{y}')\,\mathrm{d}\tilde{x}'\,\mathrm{d}\tilde{y}' \tag{5.17}$$

in analogy with Eq. (5.11), we have the expression

$$W(\tilde{x}_1,\tilde{y}_1,\tilde{x}_2,\tilde{y}_2) = \sum_{m=0}^{M} \alpha_m \phi_m^*(\tilde{x}_1,\tilde{y}_1)\phi_m(\tilde{x}_2,\tilde{y}_2) \tag{5.18}$$

for the image-plane CSD. The spectral density in the image plane, which one is usually interested in, is therefore

$$S(\tilde{x},\tilde{y}) = \sum_{m=0}^{M} \alpha_m |\phi_m(\tilde{x},\tilde{y})|^2. \tag{5.19}$$

Once the coherent modes of the incident field have been found and coherent modes up to index M to represent the incident field with sufficient accuracy, the computational complexity of evaluating the partially coherent image is $M+1$ times greater than that of calculating the coherent image.

The transfer function approach already described for fully coherent fields is applicable to efficient numerical evaluation of partially coherent diffraction images if the coherent-mode approach is used. Each mode is propagated to the plane A using an expression analogous to Eq. (5.6), multiplied by the pupil function, and finally propagated to the image plane using an expression analogous to Eq. (5.7).

5.2.2 Elementary-field representation

If we denote the incident elementary field centered at position $(\bar{x},\bar{y})$ by $e(\tilde{x}'-\bar{x},\tilde{y}'-\bar{y})$, the corresponding field transmitted by the object is given by

$$g(\tilde{x}'-\bar{x}',\tilde{y}'-\bar{y}) = t(\tilde{x}',\tilde{y}')e(\tilde{x}'-\bar{x},\tilde{y}'-\bar{y}) \tag{5.20}$$

We again write the CSD of the incident field in the form

$$W^{-}(\tilde{x}_1',\tilde{y}_1',\tilde{x}_2',\tilde{y}_2') = \iint_{-\infty}^{\infty} p(\bar{x},\bar{y})e^{*}(\tilde{x}_1'-\bar{x},\tilde{y}_1'-\bar{y}) \times e(\tilde{x}_2'-\bar{x},\tilde{y}_2'-\bar{y})\,\mathrm{d}\bar{x}\,\mathrm{d}\bar{y}. \tag{5.21}$$

The elementary-field spread function, which depends on the center coordinates $(\bar{x},\bar{y})$, is defined as

$$g(\tilde{x}-\bar{x},\tilde{y}-\bar{y}) = \iint_{-\infty}^{\infty} g(\tilde{x}'-\bar{x},\tilde{y}'-\bar{y})K(\tilde{x}-\tilde{x}',\tilde{y}-\tilde{y}')\,\mathrm{d}\tilde{x}'\,\mathrm{d}\tilde{y}'. \tag{5.22}$$

This function becomes space-invariant if no object is present (as in Paper I), in which case it needs to be evaluated only once.

The total image-plane CSD, which in the elementary-field representation is of the form

$$W(\tilde{x}_1, \tilde{y}_1, \tilde{x}_2, \tilde{y}_2) = \iint_{-\infty}^{\infty} p(\bar{x}, \bar{y}) g^*(\tilde{x}_1 - \bar{x}, \tilde{y}_1 - \bar{y}) \times g(\tilde{x}_2 - \bar{x}, \tilde{y}_2 - \bar{y}) \, \mathrm{d}\bar{x} \, \mathrm{d}\bar{y}. \tag{5.23}$$

Usually one is again interested in the spectral density of the partially coherent diffraction image, which is given by

$$S(\tilde{x}, \tilde{y}) = \iint_{-\infty}^{\infty} p(\bar{x}, \bar{y}) \left| g(\tilde{x} - \bar{x}, \tilde{y} - \bar{y}) \right|^2 \, \mathrm{d}\bar{x} \, \mathrm{d}\bar{y}. \tag{5.24}$$

For homogeneous incident fields (with a constant intensity distribution) we simply choose $p(\bar{x}, \bar{y}) = 1$, so we do not have to approximate such a field with, e.g., a Gaussian Schell-model beam like in the case of Mercer representation. In practise we of course use a discrete version of Eq. (5.23). The FFT algorithm and a discrete version of Eqs. (5.23) and (5.24) are used, with sufficiently dense sampling of $(\bar{x}, \bar{y})$ to achieve convergence.

5.2.3 Comparison of the methods: images of slits

In order to compare the two modal approaches described above we consider a y-invariant geometry involving a slit object width D, i.e.,

$$t(x') = \begin{cases} 1, & \text{if } |x'| \leq D/2 \\ 0, & \text{if } |x'| > D/2, \end{cases} \tag{5.25}$$

and assuming that the pupil function is of the form

$$P(k_x) = \begin{cases} 1, & \text{if } |k_x| \leq k\,\mathrm{NA} \\ 0, & \text{if } |k_x| > k\,\mathrm{NA}, \end{cases} \tag{5.26}$$

where $k = 2\pi/\lambda$ is the vacuum wave number and NA is the image-space numerical aperture of the imaging system. In the fully coherent and incoherent limits the diffraction images for spatially uniform illumination of the slit can be expressed in terms of sine integral functions [185, 186], but no simple analytical solutions seem

to exist for partially coherent illumination. Considering first the Mercer-type coherent-mode representation, we assume that the (geometrical image of) the incident field is a Gaussian Schell-model field with well-known Hermite-Gaussian modes introduced in Sect. 4.4. If $w \gg D$, the illumination of the slit is virtually uniform and the effect of partial coherence can be studied by varying the parameter σ.

Figure 5.2 illustrates numerical results on the imaging of a slit under variable coherence conditions. The slit width was chosen as $D = 20\lambda$ and we chose $w = 100\lambda$ in the model. Further, we assume that NA $= 0.25$. The blue curve corresponds to $\sigma = 40\lambda$ and the red one to $\sigma = 10\lambda$, which represents almost fully coherent and quasi-coherent cases, respectively. Strong intensity variations across the slit image are seen in these cases, which are well known to take place in coherent illumination [125]. The green curve with $\sigma = 2.5\lambda$ represents quasi-homogeneous illumination. In this case the fluctuations have already decreased significantly, though some level of 'overshoot' at the edge of the slit image is still apparent. Going below $\sigma = 2.5\lambda$ proved numerically problematic with the coherent-mode approach since then high-order Hermite–Gaussian modes with complicated, highly oscillatory spatial variations must be included, which causes numerical instabilities.

Let us next examine the elementary-field approach, assuming a uniform Gaussian-correlated source with the same coherence width σ as above. In this case the axial incident elementary field takes the (normalized) form

$$e(x') = \frac{1}{\pi^{1/4}\sqrt{\sigma_0}} \exp\left(-\frac{x'^2}{2\sigma^2}\right), \tag{5.27}$$

and the elementary-field expansion of the incident field can be constructed according to Eq. (5.20). In the elementary-field method, the discretization step of the center point locations $\bar{x}$ must be less than σ; for a slit of width D we need at least $N = [d/2\sigma_0] + 2$ sampling points, where the square brackets denote the integer part of the enclosure.

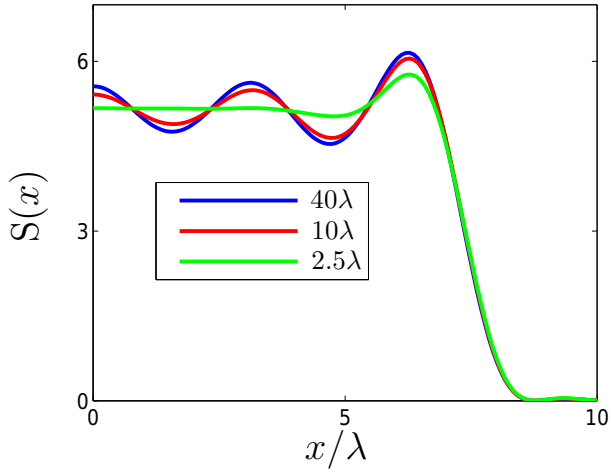

Figure 5.2: Mercer coherent-mode analysis of slit imaging under spatially partially coherent illumination. The curves are normalized with their energies $\int_0^\infty S(x)dx$. *Only one half of the slit image is shown for clarity.*

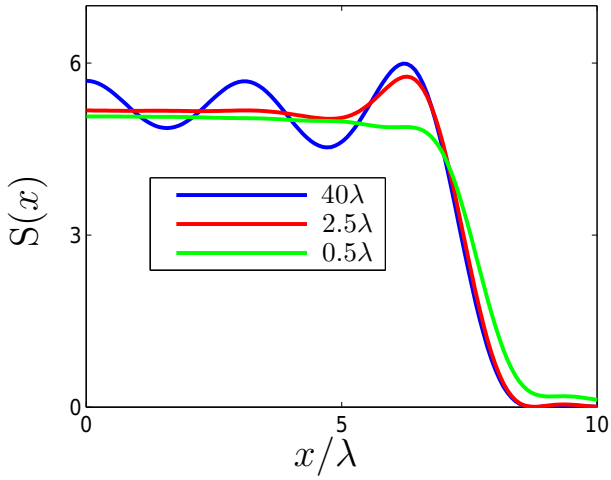

Figure 5.3: Elementary-field analysis of slit imaging with varying degrees of coherence of input illumination. The curves are normalized with their energies $\int_0^\infty S(x)dx$. *As in Fig. 5.2, only one half of the slit image is shown.*

Figure 5.3 illustrates the results of the elementary-field analysis of slit imaging with the same assumptions on the slit width and the properties of the incident field as in Fig. 5.2, but considering also

some less spatially coherent fields than those examined in Fig. 5.2. Clearly, with $\sigma = 40\lambda$ (the nearly coherent case), strong ringing effects are seen again. Also the results given by the elementary-field representation for $\sigma = 2.5\lambda$ are virtually identical with those given by the Mercer coherent-mode approach. Importantly, however, the elementary-field model allows the analysis of imaging problems with quasi-homogeneous light that may actually approach the ideal limit of full incoherence (which can not be exactly reached). The case $\sigma = 0.5\lambda$ considered in Fig. 5.2 is close to the most incoherent case that one can achieve in practice, since decreasing σ much more would lead to a non-physical situation not realizable by any condenser system. If $\sigma < 1/k\,\mathrm{NA}$, spatial-frequency components with values $k_\rho = \sqrt{k_x^2 + k_y^2} > k$, which represent evanescent waves, are required to represent the incident field precisely. Such plane-wave components can not be generated by any condenser system; the case $\sigma = 0.5\lambda$ considered in Fig. 5.3 is close to physically realizable limits even in immersion microscopes.

5.2.4 Numerical implementation with an adaptive computational window

Suppose that the effective area of the elementary field covers only a tiny part of the object around the center point $(\bar{x}, \bar{y})$, which is the case especially if the incident field is quasihomogeneous. In order to form the final image, the incident elementary field needs to be scanned over the entire object as illustrated in Fig. 5.4. It is clear that, for any arbitrary center position $(\bar{x}, \bar{y})$ of the elementary field, no new information appears in the image from regions outside a rectangle with sides $D_x \times D_y$, which essentially contains the elementary field, characterized by coherence widths $\sigma_x \times \sigma_y$ and also contains the necessary amount of zero padding to make sure that the FFT algorithm produces results with no aliasing errors. By means of numerical experiments, it has been found that the step size in scanning the elementary field needs to be $\Delta\bar{x} \times \Delta\bar{y}$, where $\Delta\bar{x} < \sigma_x$ and $\Delta\bar{y} < \sigma_y$ are chosen such that convergence of the

elementary-field superposition is ensured.

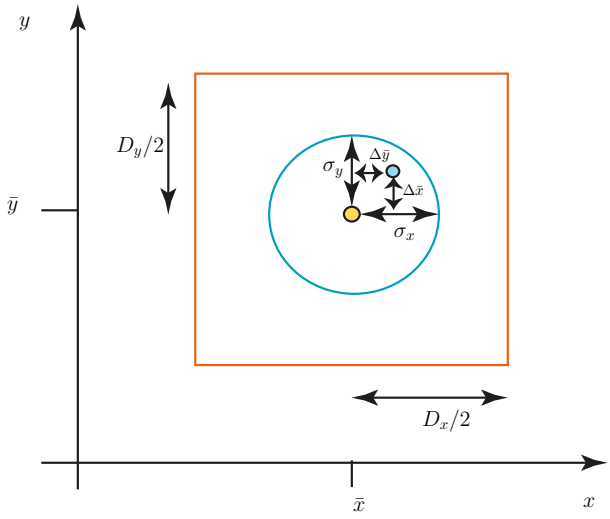

Figure 5.4: Use of an adaptive window that scans the object along with the elementary field. The yellow and blue dots represent two scanning points of the center of the elementary field, the blue circle is the effective area of the elementary field, and the red rectangle represents the corresponding computational window that is always centered at the same (discrete) point as the center of the elementary field.

If the illumination is highly coherent, the size of the elementary field is at least of the same order of magnitude as the spatial extent of the incident field. In this case the computational window must be chosen to cover the entire object and the use of adaptive windows does not help. But this is no problem since then we do not need to scan the center point position too much. On the other hand, with highly incoherent illumination, the situation is different and we need sufficient sampling within the effective area of the elementary field to represent the final image well. If we use the adaptive computational window that is shifted laterally as illustrated in Fig. 5.4, we can use the shift theorem of Fourier transforms to compute the field incident on the pupil. Hence, instead of the Fourier transform over the entire object, we only need to compute the Fourier transform over a spatially limited region around the center point of each particular elementary field to obtain the elementary-field distribu-

tion incident on the pupil at plane A. Then we multiply it with the pupil function and perform the inverse Fourier transform to obtain the elementary-field contributions to the image-plane field, which are finally summed up incoherently.

In numerical calculations we choose the discrete sampling of the center points $(\bar{x}, \bar{y})$ so that the shifts $(\Delta\bar{x}, \Delta\bar{y})$ as well as the dimensions (D_x, D_y) of the computational window are some multiples of the FFT sampling steps, so stitching the computational subfields together in the final summation of the elementary field integral pose no problems.

5.2.5 Examples: bright-field and dark-field imaging

In the examples to be presented below (as in Paper IV) we consider the standard Köhler illumination system with an incoherent primary source and a condenser [70], while previously in this chapter the illumination of the object was assumed to be of arbitrary form. We proceed to numerical demonstrations of the elementary-field decomposition technique described above by applying it to both Bright Field Imaging (BFI) and Dark Field Imaging (DFI) conditions illustrated in Fig. 5.5. Both imaging schemes can be described by assuming that an incoherent primary source is present at the input plane of the condenser. This source generates an incident field with a CSD determined by an incoherent angular correlation function with an angular spectral density of the form $S(k_x, k_y) = S_0$ when $P_1 \leq k_\rho \leq P_2$ and zero otherwise, where k_ρ is again the radial spatial frequency.

Figure 5.5 illustrates the BFI and DFI imaging geometries. In BFI, the primary source is assumed to be circular with $P_1 = 0$, such that the NA of the condenser system is determined by P_2. In DFI, an annular aperture is placed in the plane of the primary source, which blocks all directly transmitted light from passing through the pupil of radius P; thus only light scattered by the object can arrive at the image plane.

In the general case of an annular primary source, the incident

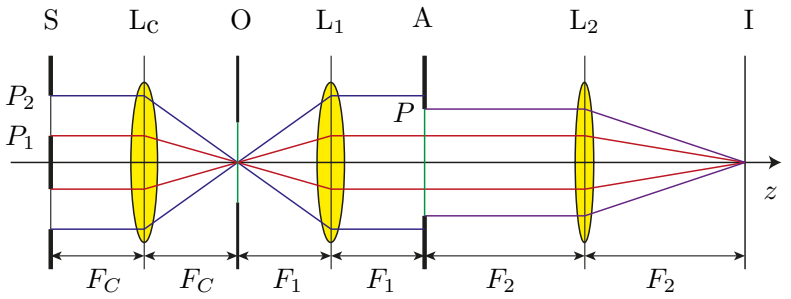

Figure 5.5: Köhler illumination of an object O with a condenser represented by a lens L_C of focal length F_C is followed by lens L_1, which forms the image of the primary source at the aperture plane A. Symbols P_1 and P_2 represent the limiting spatial frequencies generated by the annular primary source in the condenser system. Correspondingly, P denotes the maximum spatial frequency passed by the circular aperture of the imaging system. In BFI $P_1 = 0$ and in DFI $P_1 \geq P$.

elementary field may be expressed in the form

$$e_0(\boldsymbol{\rho}') = \frac{2\left[P_2 J_1(P_2\,|\boldsymbol{\rho}'|) - P_1 J_1(P_1\,|\boldsymbol{\rho}'|)\right]}{\left(P_2^2 - P_1^2\right)|\boldsymbol{\rho}'|}, \tag{5.28}$$

where J_1 is the Bessel function of the first kind and order one. In BFI we set $P_1 = 0$ and in DFI $P_1 \geq P$ as discussed above, but in both cases P_2 can vary. If the system is free from aberrations, we assume that the pupil function $P(k_x, k_y) = 1$ when $0 \leq k_\rho \leq P$. In what follows, we normalize all quantities to $P = k\,\mathrm{NA}$. The absolute value of the pupil function

$$P(k_x, k_y) = \left|P(k_x, k_y)\right| \exp\left[\mathrm{i}kW(k_x, k_y)\right] \tag{5.29}$$

accounts, as usual, for truncation and apodization of the field at the A plane. The term $W(k_x, k_y)$ contains the wave aberrations of the system, which may be expressed, e.g., by means of the Hamilton expansion [187]. The effects of aberrations on the imaging process have previously been analyzed for 1D case [188,189] and we analyze it here for 2D case, and the examples presented below give some illustrative results in the 2D case. The combined effect of spherical aberration and defocus is defined by a wave aberration function

(2D)

$$W(k_x, k_y) = a\left(k_x^2 + k_y^2\right)/P^2 + b\left(k_2^2 + k_y^2\right)^2/P^4, \tag{5.30}$$

where a and b are constants that may be chosen at will. If $a = 0$, we have pure spherical aberration and if $b = 0$ we have pure defocus in the system.

In the numerical examples that follow we consider a real-valued object shown in Fig. 5.6, which consists of the alphabets UEF. Each box superimposed on the object in the figure represents a grid with cartesian dimensions given by $r = 0.61/P$, which represents the resolution limit of the imaging system [125]. The transverse scales are in dimensionless units, the white areas have a complex-amplitude transmittance 1 and black areas have a complex-amplitude transmittance of 0.

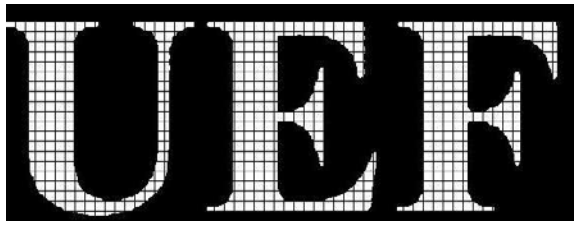

Figure 5.6: The 2D resolution target used as the object in the numerical simulations. Each box superimposed on the object represents a grid of dimensions $r = 0.61/P$ in relation to the resolution limit of the imaging system. The size of each alphabet is equal to the number of boxes occupied by the sidewalls of the alphabet.

Some results of the elementary-field analysis of BFI and DFI imaging systems without aberrations are presented in Figs. 5.7 and 5.8. The BFI results illustrate a well-known phenomenon: lowering the degree of spatial coherence (small P_2 with high spatial coherence to a large P_2 with low spatial coherence) results in a reduction of speckle-like fluctuations in the image-plane intensity profile and resolution of the image is improved. The edge enhancement effects in DFI imaging are clearly seen in Fig. 5.8, which are reduced by lowering the degree of spatial coherence.

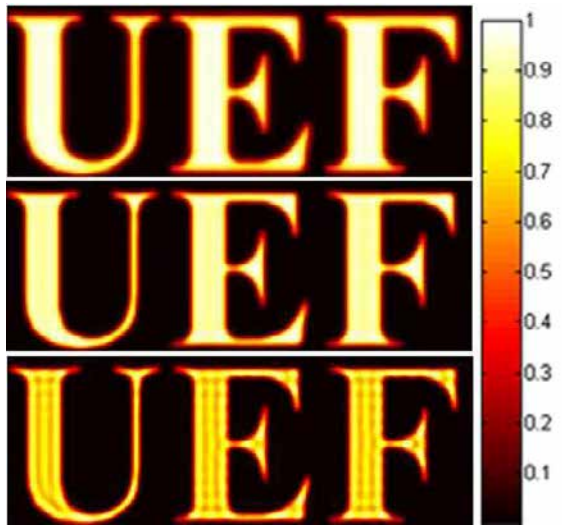

Figure 5.7: Bright-field imaging ($P_1 = 0$) of a UEF resolution target. Top: $P_2 = 2P$. Middle: $P_2 = 0.7P$. Bottom: $P_2 = 0.1P$. As the spatial coherence is lowered ($P_2 = 0.1P$ to $P_2 = 2P$), the resolution of image is improved.

The effect of defocusing and spherical aberration on the image quality in both BFI and DFI conditions is illustrated in Fig. 5.9. Here we assume one wave of pure spherical aberration ($b = 1$) to be present in the system and consider the effect of defocusing by varying the value of a in Eq. (5.30). The results illustrate well how a suitable amount of defocusing can balance the image-deteriorating effect of spherical aberration, at least to some extent [187].

More examples on numerical application of the elementary-field model to imaging problems can be found in Paper IV. The media files presented there illustrate more closely the effects of variable partial coherence on the image quality of aberration-free bright-field and dark-field imaging systems, as well as the effects of defocusing in the image quality of systems with spherical aberration.

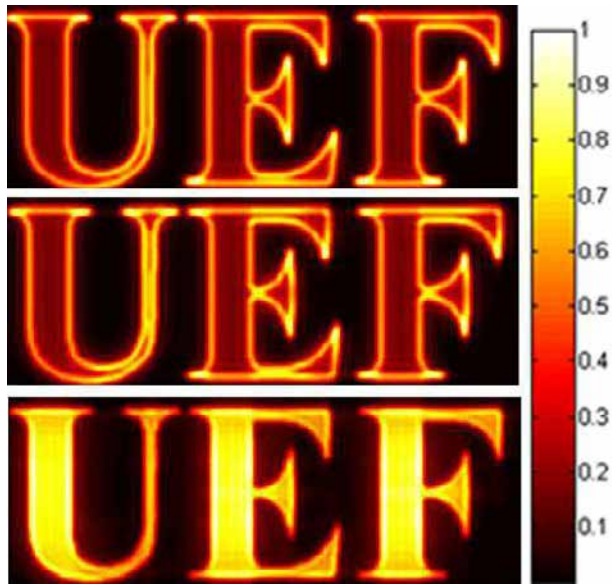

Figure 5.8: Dark-field imaging ($P_1 = P$). Top: $P_2 = 2P$. Middle: $P_2 = 1.6P$. Bottom: $P_2 = 1.1P$. As the spatial coherence is lowered ($P_2 = 1.1P$ to $P_2 = 2P$), the resolution of image is improved.

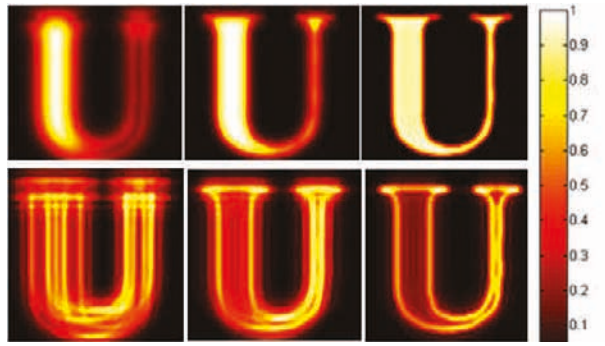

Figure 5.9: The effect of defocusing in bright-field imaging (top row) with $P_1 = 0$ and $P_2 = 0.7P$. Left: $a = 0$. Center: $a = -0.75$. Right: $a = -1$. Bottom row: Dark-field imaging with $P_1 = P$ and $P_2 = 1.6P$. Left: $a = 0$. Center: $a = -0.75$. Right: $a = -1$. For clarity only one alphabet U is shown.

5.3 SUMMARY

In this chapter we have considered imaging systems under partially coherent illumination conditions. Modal methods for wave optical

analysis of image formation in such systems were studied, which permit efficient numerical evaluation of partially coherent diffraction images of arbitrary objects. Particular attention was paid to the elementary-field approach, which is applicable to any illumination conditions allowed by the Schell-model assumption on the angular correlation function of the illuminating field [52, 138, 139, 152]. Examples on slit imaging, and on bright-field and dark-field imaging of a complicated object, were presented to demonstrate the effects of partial coherence on image formation and the numerical feasibility of the elementary-field model.

6 Discussion and conclusion

Three different types of beam-shaping elements have been theoretically analyzed in this thesis. The method for designing them by means of geometrical optics was also discussed in brief. The emphasis has been on the formulation and interpretation of how these elements perform on the basis of diffraction theory when illuminated either by stationary or non-stationary light. It was shown that, when the elements are illuminated with nearly coherent illumination, the target intensity profiles exhibit edge and color distortion effects. Such effects are reduced if the degree of spatial coherence of the illuminating fields is decreased. Secondly it was highlighted that, contrary to common belief, conventional or harmonic diffractive beam shaping elements can be used to shape beams radiated by polychromatic sources with spectral extensions of tens of nanometers. Harmonic diffractive beam shaping elements were shown to be useful even for highly broadband sources like RGB or supercontinuum.

Two modal approaches, namely the Mercer coherent-mode representation and the elementary field representation, were applied to partially coherent stationary and non-stationary fields. These representations decrease the computational complexity of modeling partially coherent field in various situations. When the modal approach was used for beam shaping, individual coherent modes produced Fourier plane intensity profiles of strongly different shapes but their superposition showed a good approximation of the desired flat-top profile. These concepts were also illustrated using Gaussian Schell-model fields in space-frequency and space-time domains, for shaping pulsed beams (non-stationary fields). The target plane space–frequency intensity distribution showed good quality flat-top profiles with smooth edges. The space–time pulse profiles were seen to possess bent shapes, implying that the axial part of the pulse is seen first at the target plane and the on-axis pulse has

in fact passed before any light arrives at the edges. This behavior is common to model sources and real light sources including supercontinuum, and it can be of importance in time resolved experiments.

In Chapter 5, we concentrated on the computational effort required for partially coherent imaging, demonstrating the possibility of reducing it by representing the incident CSD in terms of spatially shifted and mutually uncorrelated elementary field modes. We showed that this elementary-field model (introduced in Paper IV) is not restricted to incoherent primary sources but can be applied to any spatially partially coherent primary sources that obey the spatial Schell model. Examples on bright-field and dark-field imaging of a 2D resolution target were presented to illustrate the effect of varying the degree of spatial coherence in the imagery of the resolution target. The elementary-field model was compared to the Mercer modal expansion in the case of imaging of a 1D slit and shown to outperforms the latter especially if illumination with a low degree of spatial coherence is considered.

All studies in this thesis have been done in the framework of scalar coherence theory, and hence the results are more or less restricted to the paraxial domain, which is the standard approach adopted in Fourier optics. Non-paraxial analysis, where the electromagnetic nature of light must be taken into account, is however becoming increasingly relevant. The paraxial scalar approach taken here is reasonably valid if we consider beamlike fields with divergence angles below 10-15 degrees, but if the beam divergence exceeds this region, the longitudinal components of the electromagnetic field become increasingly significant and the optical fields should be described electromagnetically when free-space propagation, beam shaping, or imaging problems are considered.

In beam shaping problems it is no major problem to extend the analysis into the non-paraxial domain as long as the thin-element approximation can be assumed to hold. However, if the angular extent of the signal (such as a flat-top profile) to be generated in the far field exceeds $\sim 30^\circ$, the thin-element approximation begins

to fail at least if diffractive elements are employed [190–192]. In such circumstances the element response should be analyzed by rigorous electromagnetic diffraction theory, and this is indeed one natural extension of the work presented above.

In the treatment of imaging problems (bright-field and dark-field) the discussion was also limited to the scalar theory of partially coherent fields and in the thin-element approximation of the object response. If the thin-element approximation is retained, the analysis could rather easily be extended to electromagnetic fields in the non-paraxial domain. Again the longitudinal components of the electromagnetic field would contribute to the results and certain geometrical factors appear, which can be neglected in paraxial analysis but must be included in the non-paraxial treatment [193].

One major extension of the results presented in this thesis would be the abandoning of the thin-element approximation, implying that the response of the object to the illuminating partially coherent field would be considered rigorously, such as using the Fourier Modal Method (FMM) [194]. There are several alternative approaches of doing this, but it appears that the key to all of them is to first evaluate the scattering matrix (S-matrix) of a given object. Once this computationally heavy task is performed at a sufficient precision, the response of the object to any fully coherent field (such as the elementary field mode) can be evaluated by simple matrix multiplication and the rest of the analysis could be performed in much the same way as described in Chapter 5 and Paper IV.

References

[1] L. Mandel and E. Wolf, *Optical Coherence and Quantum Optics* (Cambridge University Press, 1995).

[2] E. L. O. Neill, *Introduction to Statistical Optics* (Courier Corporation, 2004).

[3] E. Wolf, "Optics in terms of observable quantities," *Il Nuovo Cimento* **12**, 884–888 (1954).

[4] E. Wolf, "A macroscopic theory of interference and diffraction of light from finite sources. I. Fields with a narrow spectral range," *Proc. Roy. Soc. London. A: Mathem. Phys. and Eng. Sci.* **225**, 96–111 (1954).

[5] M. Bertolotti, L. Sereda, and A. Ferrari, "Application of the spectral representation of stochastic processes to the study of nonstationary light radiation: a tutorial," *Pure Appl. Opt.* **6**, 153–171 (1997).

[6] M. Bertolotti, A. Ferrari and L. Sereda, "Coherence properties of nonstationary polychromatic light sources," *J. Opt. Soc. Am. B* **12**, 341–347 (1995).

[7] L. Sereda, M. Bertolotti, and A. Ferrari, "Coherence properties of nonstationary light wave fields," *J. Opt. Soc. Am. A* **15**, 695–705 (1998).

[8] N. C. Roberts, "Beam shaping by holographic filters," *Appl. Opt.* **28**, 31–32 (1989).

[9] M. A. Golub, I. N. Sisakyan, and V. A. Soifer, "Infra-red radiation focusators," *Opt. Laser Eng.* **15**, 297–309 (1991).

[10] W. Singer, H. P. Herzig, M. Kuittinen, E. Piper, and J. Wangler, "Diffractive beamshaping elements at the fabrication limit," *Opt. Eng.* **35**, 2779–2787 (1996).

[11] H. Aagedal, M. Schmid, S. Egner, J. Müller-Quade, T. Beth, and F. Wyrowski, "Analytical beam shaping with application to laser-diode arrays," *J. Opt. Soc. Am. A* **14**, 1549–1553 (1997).

[12] J. Jia, C. Zhou, X. Sun, and L. Liu, "Superresolution laser beam shaping," *Appl. Opt.* **43**, 2112–2117 (2004).

[13] W. Mohammed and X. Gu, "Long-period grating and its application in laser beam shaping in the 1:0m wavelength region," *Appl. Opt.* **48**, 2249–2254 (2009).

[14] R. Pereira, B. Weichelt, D. Liang, P. J. Morais, H. Gouveia, M. Abdou-Ahmed, A. Voss, and T. Graf, "Efficient pump beam shaping for high-power thin-disk laser systems," *Appl. Opt.* **49**, 5157–5162 (2010).

[15] O. Bryndahl, "Optical map transformation," *Opt. Commun.* **10**, 164–169 (1974).

[16] E. B. Kley, L. C. Wittig, M. Cumme, U. D. Zeitner, P. Dannberg, "Fabrication and properties of refractive micro optical beam shaping elements," *Proc. SPIE* **3879**, 20–31 (1999).

[17] J. Choi, H. Kong, and J. Lee, "Optical design of a refractive beam shaper that transforms a Gaussian beam profile into a diverging uniform line beam profile," *Proc. SPIE* **055101** (2013).

[18] P. J. Smilie and T. J. Suleski, "Variable-diameter refractive beam shaping with freeform optical surfaces," *Opt. Lett.* **36**, 4170–4172 (2011).

[19] P. W. Rhodes and D. L. Shealy, "Refractive optical systems for irradiance redistribution of collimated radiation: their design and analysis," *Appl. Opt.* **19**, 3545–3553 (1980).

[20] S. Zhang, G. Neil, and M. Shinn, "Single-element laser beam shaper for uniform flat-top profiles," *Opt. Express* **11**, 1942–1948 (2003).

[21] J. A. Hoffnagle and C. M. Jefferson, "Design and performance of a refractive optical system that converts a Gaussian to a flattop beam," *Appl. Opt.* **39**, 5488–5499 (2000).

[22] J. J. Kasinski and R. L. Burnham, "Near-diffraction-limited laser beam shaping with diamond-turned aspheric optics," *Opt. Lett.* **22**, 1062–1064 (1997).

[23] D. M. Dagenais, J. A. Woodroffe, and I. Itzkan, "Optical beam shaping of a high power laser for uniform target illumination," *Appl. Opt.* **24**, 671–675 (1985).

[24] Y. Xia, C. Ke-Qiu, and Z. Yan, "Optimization design of diffractive phase elements for beam shaping," *Appl. Opt.* **50**, 5938–5943 (2011).

[25] W. Qu, H. Gu, Q. Tan, and G. Jin, "Precise design of two-dimensional diffractive optical elements for beam shaping," *Appl. Opt.* **54**, 6521–6525 (2015).

[26] J. S. Liu and M. R. Taghizadeh, "Iterative algorithm for the design of diffractive phase elements for laser beam shaping," *Opt. Lett.* **27**, 1463–1465 (2002).

[27] X. Tan, B. Y. Gu, G. Z. Yang, and B. Z. Dong, "Diffractive phase elements for beam shaping: a new design method," *Appl. Opt.* **34**, 1314–1320 (1995).

[28] C.Y. Han, Y. Ishii, and K. Murata, "Reshaping collimated laser beams with Gaussian profile to uniform profiles," *Appl. Opt.* **22**, 3644–3647 (1983).

[29] W. B. Veldkamp, "Laser beam profile shaping with interlaced binary diffraction gratings," *Appl. Opt.* **21**, 3209–3212 (1982).

[30] J. Cordingley, "Application of a binary diffractive optic for beam shaping in semiconductor processing by lasers," *Appl. Opt.* **32**, 2538–2542 (1993).

[31] G. Q. Zhang, B. Y. Gu, and G. Z. Yang, "Design of diffractive phase elements that produce focal annuli: a new method," *Appl. Opt.* **34**, 8110–8115 (1995).

[32] J. Bengtsson, "Kinoform-only Gaussian-to-rectangle beam shaper for a semiconductor laser," *Appl. Opt.* **35**, 3807–3814 (1996).

[33] K. Miyamoto, "The phase Fresnel lens," *J. Opt. Soc. Am.* **51,** 17–20 (1961).

[34] T. Stone and N. George, "Hybrid diffractive-refractive lenses and achromats," *Appl. Opt.* **27**, 2960–2971 (1988).

[35] C. Londoño and P. P. Clark, "Modeling diffraction efficiency effects when designing hybrid diffractive lens systems," *Appl. Opt.* **31**, 2248–2252 (1992).

[36] G. P. Behrmann, J. N. Mait, "Hybrid (refractive/diffractive) optics," in *Micro-Optics: Elements, Systems and Applications*, H. P. Herzig, ed. (Taylor & Francis, London, 1997), pp. 259292.

[37] D. C. O'Shea, T. J. Suleski, A. D. Kathman and D. W. Prather *Diffractive Optics: Design, Fabrication, and Test* (Chapters 4 and 10, SPIE, 2004).

[38] Herzig, H. P., *Micro-Optics: Elements, Systems And Applications* (Chapter 10, Taylor & Francis, 1997).

[39] A. P. Wood, "Design of infrared hybrid refractive-diffractive lenses," *Appl. Opt.* **31**, 2253–2258 (1992).

[40] R. H. Katyl, "Compensating Optical Systems. Part1: Broadband Holographic Reconstruction," *Appl. Opt.* **11**, 1241–1247 (1972).

[41] R. H. Katyl, "Compensating Optical Systems. Part 2: Generation of Holograms with Broadband Light," *Appl. Opt.* **11**, 1248–1254 (1972).

[42] J. Lancis, G. M. Vega, E. Tajahuerce, V. Climent, P. Andrs, and J. Caraquitena, "Chromatic compensation of broadband light diffraction: ABCD-matrix approach," *J. Opt. Soc. Am. A* **21**, 1875–1885 (2004).

[43] F. Gori and R. Grella, "Shape invariant propagation of polychromatic fields," *Opt. Commun.* **49**, 173–177 (1984).

[44] E. Wolf, "Invariance of the spectrum of light on propagation," *Phys. Rev. Lett.* **56**, 1370–1372 (1986).

[45] E. Wolf and D. F. V. James, "Correlation-induced spectral changes," *Rep. Prog. Phys.* **59**, 771–818 (1996).

[46] E. Wolf, "New spectral representation of random sources and of the partially coherent fields that they generate," *Opt. Commun.* **38**, 3–6 (1981).

[47] G. S. Agrawal and E. Wolf, "Higher-order coherence function in the space-frequency domain," *J. Mod. Opt.* **40**, 1489–1496 (1993).

[48] E. Wolf, "New theory of partial coherence in the space-frequency domain. Part II: Steady state fields and higher order correlations," *J. Opt. Soc. Am.* **3**, 76–85 (1986).

[49] E. Wolf, "New theory of partial coherence in the space-frequency domain. Part I: Spectra and cross-spectra of steady-state sources," *J. Opt. Soc. Am.* **7**, 343–351 (1982).

[50] F. Riesz and B. S. Nagy, *Functional Analysis* (Dover, 1990), Chapter VI.

[51] J. Turunen, "Elementary-field representations in partially coherent optics," *J. Mod. Opt.* **58**, 509–527 (2010).

[52] A. Burvall, A. Smith, and C. Dainty, "Elementary functions: propagation of partially coherent light," *J. Opt. Soc. Am. A* **26,** 1721–1729 (2009).

[53] A. Smith, and C. Dainty, "Numerical modelling of spatial coherence using the elementary function method," *App. Opt.* **52**, 2815–2827 (2013).

[54] D. Gabor, "Theory of communication," *J. Inst. of Elect. Eng.* **93**, 429–457 (1946).

[55] E. Wolf, *Introduction to Theory of Coherence and Polarization of Light* (Cambridge University Press, Cambridge, 2007).

[56] D. G. Lampard, "Generalization of the WienerKhintchine Theorem to Nonstationary Processes," *J. Appl. Phys.* **25**, 802–803 (1954).

[57] W. Lu, and N. Vaswani "The Wiener-Khinchin Theorem for Non-wide Sense stationary Random Processes," *J. Appl. Phys.* **25**, 802–803 (1954).

[58] W. A. Gardner, "A sampling theorem for nonstationary random processes," *IEEE* **18**, 808–809 (1972).

[59] J. G. Proakis and M. Salehi, *Communication Systems Engineering*(Prentice Hall, 2001).

[60] P. Z. Peebels, *Probability,Random Variables and Random Signal Principles* (McGraw-Hill Publishing Company, 2001).

[61] A. P. Suppappola, *Applications in Time-Frequency Signal Processing* (Taylor and Francis Group, CRC Press, 2003).

[62] N. Wiener, "Generalized harmonic analysis," *Acta Math.* **55**, 117–258 (1930).

[63] A. Khintchine, "Korrelationstheorie der stationären stochastischen prozesse," *Math. Ann.* **109**, 604–615 (1952).

[64] R. D. Yates and D. J. Goodman, *Probablity and Stochastic Processez: A Friendly Introduction for Electrical and Computer Engineers* (Wiley, 2005).

[65] C. W. Billings and J. Tabak, *Lasers: The Technology and Uses of Crafted Light* (Facts On File, 2006).

[66] L. Mandel and E. Wolf, "Complete coherence in the space-frequency domain," *Opt. Comm.* **36**, 247–249 (1981).

[67] W. H. Carter, "Difference in the definitions of coherence in the space-time domain and in the space-frequency domain," *J. Modern. Opt.* **39**, 1461–1470 (1992).

[68] K. Saastamoinen, J. Turunen, P. Vahimaa and A. T. Friberg, "Spectrally partially coherent propagation-invariant fields," *Phys. Rev. A.* **80**, 053804 (2009).

[69] R. Dutta, M. Korhonen, A. T. Friberg, G. Genty, and J. Turunen, "Broadband spatiotemporal Gaussian Schell-model pulse trains," *J. Opt. Soc. Am. A* **31**, 637–643 (2014).

[70] M. Born and E. Wolf, *Principles of Optics: Electromagnetic Theory of Propagation, Interference and Diffraction of Light* (Cambridge University Press, 1999).

[71] P. W. Milonni and J. H. Eberly, *Lasers* (Wiley, 1988).

[72] P. W. Milonni and J. H. Eberly, *Lasers Physics* (Wiley, 2010).

[73] R. C. Coutinho, "Variable numerical-aperture temporal-coherence measurement of resonant-cavity LEDs," *IEEE J. Lightwave Tech.* **21**, 149–154 (2003).

[74] N. Stelmakh and M. Flowers, "Measurement of spatial modes of broad-area diode Lasers with 1-GHz resolution grating spectrometer," *IEEE Photon. Technol. Lett.* **18**, 1618–1620 (2006).

[75] N. Stelmakh, "Harnessing multimode broad-area daser-diode emission into a single-lobe diffraction-limited spot," *IEEE Photon. Technol. Lett.* **19**, 1392–1394(2007).

[76] N. Stelmakh, "Combining of modes of broad-area laser diode into a single-mode spot," *IEEE Lasers and Electro-Optics* 1–2 (2007).

[77] R. J. Lang, G. Larsson, and J. G. Cody, "Lateral modes of broad area semiconductor lasers: Theory and Experiment," *IEEE J. Quantum Electronics* **27**, 312–320(1991).

[78] T. Burkhard, M. O. Ziegler, I. Fischer and W. Elsser, "Spatio-temporal dynamics of broad area semiconductor lasers and its characterization," *Chaos, Solitons & Fractals* **10**, 845–850(1999).

[79] I. Fischer, O. Hess, W. Elsser and E. Göbel, "Complex spatio-temporal dynamics in the near-eld of a broad-area semiconductor laser," *Europhys. Lett.* **35**, 579–584(1996).

[80] M. O. Ziegler, M. Münkel, T. Burkhard, G. Jennemann, I. Fischer and W. Elsäer "Spatiotemporal emission dynamics of ridge waveguide laser diodes: picosecond pulsing and switching," *J. Opt. Soc. Am. B* **16**, 2015–2022 (1999).

[81] A. Valle and L. Pesquera, "Analytical calculation of transverse mode characteristics in vertical-cavity surfaceemitting lasers," *J. Opt. Soc. Am. B* **19**, 1549-1557 (2002).

[82] T. Gensty, K. Becker, I. Fischer,W. Elsäer, C. Degen, P. Debernardi, and G. P. Bava, "Wave chaos in real-world vertical-cavity surface-emitting laser," *Phys. Rev. Lett.* **94**, 233901 (2005).

[83] M. Peeters, G. Verschaffelt, H. Thienpont, S. K. Mandre, and I. Fischer "Spatial decoherence of pulsed broad-area vertical-cavity surface-emitting lasers," *Opt. Express* **13**, 9337–9345 (2005).

[84] H. J. Yoo, J. R. Hayes, E. G. Paek, A. Scherer, and Y.-S. Kwon," Array mode analysis of two-dimensional phased arrays of vertical-cavity surface-emitting lasers," *IEEE J. Quantum Electron.* **26**, 1039–1051 (1990).

[85] M. Gower, P. T. Rumsby, D. T. Thomas, "Novel applications of excimer lasers for fabricating biomedical and sensor prod-

ucts, in Excimer Lasers: Applications, Beam Delivery Systems, and Laser Design," *Proc. SPIE* **1835**, 133-142 (1993).

[86] T. Znotins, "Industrial applications of excimer lasers," in *Excimer Lasers and Optics*, T. S. Luk, ed., *Proc. SPIE* **710**, 55-62 (1986).

[87] F. Nikolajeff, S. Hard, and B. Curtis, "Diffractive microlenses replicated in fused silica for excimer laser-beam homogenizing," *Appl. Opt.* **36**, 8481–8489 (1997).

[88] M. N. Hasan and Y. C. Lee, "Beam pen lithography based on focused laser diode beam with single microlens fabricated by excimer laser," *Opt. Express* **23**, 4494–4505 (2015).

[89] S. Kawata, I. Hikima, Y. Ichihara, S. Watanabe, "Spatial coherence of KrF excimer lasers," *Appl. Opt.* **31**, 387-396 (1992).

[90] G. Genty, S. Coen, and J. M. Dudley, "Fiber supercontinuum sources," *J. Opt. Soc. Am. B* **24**, 1771-1785 (2007).

[91] J. M. Dudley and S. Coen, "Coherence properties of supercontinuum spectra generated in photonic crystal and tapered optical fibers," *Opt. Lett.* **27**, 1180-1182 (2002).

[92] J. M. Dudley, and S. Coen, "Numerical simulations and coherence properties of supercontinuum generation in photonic crystal and tapered optical fibers," *IEEE J. Sel. Top. Quantum Electron.* **8**, 651-659 (2002).

[93] G. Genty, M. Surakka, J. Turunen, and A. T. Friberg, "Second-order coherence of supercontinuum light," *Opt. Lett.* **35**, 3057-3059 (2010).

[94] G. Genty, M. Surakka, J. Turunen, and A. T. Friberg, "Complete characterization of supercontinuum coherence," *J. Opt. Soc. Am. B* **28**, 2301–2309 (2011).

[95] J. M. Dudley and J. R. Taylor, eds., *Supercontinuum Generation in Optical Fibers* (Cambridge University, 2010).

[96] B. W. J. McNeil, and N. R. Thompson, "X-ray free-electron lasers," *Nature Ptotonics* **4**, 814–821(2010).

[97] J. Feldhaus, J. Arthur and J. B. Hastings, "X-ray free-electron lasers," *J. Phys. B: At. Mol. Opt. Phys.* **38**, S799–S819 (2005).

[98] I. A. Vartanyats and A. Singer, "Temporal and spatial coherence properties of free-electron laser pulses in the extreme ultraviolet region," *Phys. Rev. Spec. Topics – Accel. Beams* **14**, 080701 (2011).

[99] I. A. Singer, A. Vartanyats, M. Kuhlmann, S. Dusterer, R. Treusch, and J. Feldhaus, "Transverse-coherence properties of the free-electron-laser FLASH at DESY," *Phys. Rev. Lett.* **101**, 254801 (2008).

[100] I. A. Vartanyats, A. P. Mancuso, A. Singer, O. M. Yefanov, and J. Gulden. "Coherence measurements and coherent diffractive imaging at FLASH," *J. Phys. B: Mol. Opt. Phys.* **43**, 194016 (2010).

[101] I. A. Vartanyats *et al.* "Coherence Properties of Individual Femtosecond Pulses of an X-Ray Free-Electron Laser," *Phys. Rev. Lett.* **107**, 144801 (2011).

[102] R. Mitzner *et al*,, "Spatio-temporal coherence of free electron laser pulses in the soft X-ray regime," *Opt. Express* **16**, 19909–19919 (2008).

[103] E. L. Saldin, E. A. Schneidmiller, and M. V. Yurkov, "Coherence properties of the radiation from X-ray free electron laser," *Opt. Comm.* **281**, 1179–1188(2007).

[104] E. L. Saldin, E. A. Schneidmiller, and M. V. Yurkov, "Statistical and coherence properties of radiation from x-ray free-electron lasers," *New J. Phys.* **12**, 035010(2010).

[105] I. A. Vartanyats and A. Singer "Coherence properties of hard x-ray synchrotron sources and x-ray free electron lasers,"*New J. Phys.* **12**, 035004 (2010).

[106] I. A. Singer *et al*,, "Spatial and temporal coherence properties of single-free electron laser pulses," *Opt. Express* **20**, 17480–17495 (2012).

[107] J. Turunen, and F. Wyrowski, eds, *Diffractive Optics for Industrial and Commercial Applications* (Akademic-Verlag, Berlin, 1997), Chapter 6.

[108] E. B. Kley, M. Cumme, L. C. Wittig, M. Thieme and W. Gabler, "Beam shaping elements for holographic applications," *Proc. SPIE* **4179**, 58–64 (2000).

[109] D. L. Shealy, F. M. Dickey and S. C. Holswade, *Laser Beam Shaping Applications* (CRC Press, 2005).

[110] G. Raciukaitis, E. Stankevicius, P. Gecys, M. Gedvilas, C. Bischoff, E. Jaeger, U. Umhofer and F. Volklein "Laser processing by using diffractive optical laser beam shaping technique," *J. Laser Micro/Nanoengineering* **6**, 37–43 (2011).

[111] O. Homburg, D. Hauschild, F. Kubacki, and V. Lissotschenko, "Efficient beam shaping for high-power laser applications," *Proc. SPIE* **6216**, 621–608 (2006).

[112] C. N. Kurtz, H. O. Hoadley, and J. J. DePalma, "Design and synthesis of random phase diffusers," *J. Opt. Soc. Am.* **68**, 1080–1092 (1973).

[113] O. Bryngdahl, "Geometrical transformations in optics," *J. Opt. Soc. Am.* **64**, 1092–1099 (1974).

[114] N. C. Roberts, "Multilevel computer-generated holograms with separable phase functions for beam shaping," *Appl. Opt.* **31,** 3198 (1992).

[115] F. M. Dickey and S. C. Holswade, *Laser Beam Shaping: Theory and Techniques* (Marcel Dekker, 2000).

[116] B. R. Frieden, "Lossless conversion of a plane laser wave to a plane wave of uniform irradiance," *App. Opt.* **4**, 1400–1403 (1965).

[117] D. L. Shealy, and J. A. Hoffnagle, "Laser beam shaping profiles and propagation," *App. Opt.* **45**, 5118–5131 (2006).

[118] L. A. Romero and F. M. Dickey, "Lossless laser beam shaping," Opt. Eng. **13,** 751–760 (1996).

[119] F. Wyrowski and O. Bryngdahl, "Iterative Fourier-transform algorithm applied to computer holography," *J. Opt. Soc. Am. A* **5**, 1058–1065 (1988).

[120] O. Ripoll, V. Kettunen, H. P. Herzig, "Review of iterative Fourier-transform algorithms for beam shaping applications," *J. Opt. Soc. Am. A* **43,** 2549–2556 (2004).

[121] D. Faklis and G. M. Morris, "Spectral properties of multiorder diffractive lenses," *Appl. Opt.***34,** 2462–2468 (1995).

[122] D. W. Sweeney and G. E. Sommargren, "Harmonic diffractive lenses," *Appl. Opt.* **34,** 2469–2475 (1995).

[123] A. Forbes, F. Dickey, M. DeGama, and A. d. Plessis "Wavelength tunable laser beam shaping," *Opt. Lett.* **37**, 49–51 (2012).

[124] B. Mercier, J. P. Rousseau, A. Jullien, and L. Antonucci "Nonlinear beam shaper for femtosecond laser pulses, from Gaussian to flat-top profile," *Opt. Commun.* **283**, 2900–2907 (2010).

[125] J. W. Goodman, *Introduction to Fourier Optics* (McGraw-Hill, New York, 1968).

[126] F. M. Dickey, and S. C. Holswade, "Gaussian laser beam profile shaping," *Opt. Eng.* **35,** 3285–3295 (1996).

[127] S. Sahin and O. Korotkova, "Light sources generating far fields with tunable flat profiles," *Opt. Lett.* **37**, 2970-2972 (2012).

[128] W.-H. Lee, "Computer-generated holograms: techniques and applications," in *Progress in Optics* XVI, E. Wolf, ed. (North-Holland, 1978), pp. 119–223.

[129] S. N. Kasarova *et al.*, "Analysis of the dispersion of optical plastic materials," *Opt. Mater.* **29,** 1481–1490 (2007).

[130] E. Wolf, "New spectral representation of random sources and the partially coherent fields they generate," *Opt. Commun.* **38**, 3–6 (1981).

[131] A. Starikov and E. Wolf, "Coherent-mode representation of Gausssian Schell-model fields and radiation fields," *J. Opt. Soc. Am.A* **72**, 923–927 (1982).

[132] E. Wolf, "Coherent-mode propagation in spatially band-limited wave fields," *J. Opt. Soc. Am. A* **3**, 1920–1924 (1984).

[133] H. Lajunen, J. Tervo, and P. Vahimaa, "Overall coherence and coherent-mode expansion of spectrally partially coherent plane-wave pulses," *J. Opt. Soc. Am. A* **21**, 2117–2123 (2005).

[134] H. Lajunen, J. Tervo, and P. Vahimaa, "Theory of spatially and spectrally partially coherent pulses," *J. Opt. Soc. Am. A* **22**, 1536–1545 (2005).

[135] Lajunen, H. and A. T. Friberg, "Quasi-stationary plane-wave optical pulses and the van CittertZernike theorem in time," *J. Opt. Soc. Am. A* **23**, 2530–2537 (2006).

[136] F. Gori, "Collett-Wolf sources and multimode lasers," *Opt. Commun.* **34**, 301–305 (1980).

[137] F. Gori, "Mode propagation of the fields generated by Collett–Wolf Schell-model sources," *Opt. Commun.* **46**, 149–154 (1983).

[138] P. Vahimaa and J. Turunen, "Finite-elementary-source model for partially coherent radiation," *Opt. Express* **14**, 1376–1381 (2006).

[139] J. Tervo, J. Turunen, P. Vahimaa, and F. Wyrowski, "Shifted-elementary-mode representation for partially coherent vectorial fields," *J. Opt. Soc. Am. A* **27**, 2004–2014 (2010).

[140] T. Alieva, J. A. Rodrigo, A. Cmara, and E. Abramochkin, "Partially coherent stable and spiral beams," *J. Opt. Soc. Am. A* **30**, 2237–2243 (2013).

[141] H. Partanen, J. Turunen, and J. Tervo, "Coherence measurement with digital micromirror device," *Opt. Lett.* **39**, 1034–1037 (2014).

[142] H. Partanen, N. Sharmin, J. Tervo, and J. Turunen, "Specular and antispecular light beams," *Opt. Express* **23**, 28718–28727 (2015).

[143] H. Partanen, J. Tervo, and J. Turunen, "Coupling of spatially partially coherent beams into planar waveguides," *Opt. Express* **23**, 7879-7893 (2015).

[144] H. Partanen, J. Tervo, and J. Turunen, "Spatial coherence of broad-area laser diodes," *Appl. Opt.* **52**, 3221–3228 (2013).

[145] J. Turunen, "Low coherence laser beams," in *Laser Beam Propagation: Generation and Propagation of Customized Light*, A. Forbes, Ed. (CRC Press, 2014).

[146] J. Deschamps, D. Courjon, and J. Bulabois, "Gaussian Schell-model sources: an example and some perspectives," *J. Opt. Soc. Am.* **73**, 256–261 (1983).

[147] J. T. Foley, "The directionality of gaussian Schell-model beams," *Opt. Commun.* **26**, 297–300 (1978).

[148] Q. He, and J. Turunen, "Propagation and imaging experiments with Gaussian Schell-model beams," *Opt. Commun.* **67**, 245–250 (1988).

[149] E. Collett and E. Wolf, "Beams generated by Gaussian quasi-homogeneous sources," *Opt. Commun.* **32**, 27–31 (1980).

[150] J. D Farina, L. M. Narducci and E. Collett , "Generation of highly directional beams from a globally incoherent source," *Opt. Commun.* **32**, 203–207 (1980).

[151] A. T. Friberg, and R. J. Sudol , "Propagation parameters of gaussian Schell-model beams," *Opt. Commun.* **41**, 383–387 (1982).

[152] F. Gori and C. Palma, "Partially coherent sources which give rise to highly directional laser beams," Opt. Commun. **27,** 185–188 (1978).

[153] F. Gori,"Directionality and spatial coherence," *Opt. Acta* **27**, 1025–1034 (1980).

[154] P. Paakkonen, J. Turunen, P. Vahimaa, A. Friberg, F. Wyrowski, "Partially coherent Gaussian pulses," *Opt. Commun.* **204**, 53–58 (2002).

[155] B. Lacaze, "About the Gaussian-Schell pulse train spectrum," *Opt. Exp.* **15**, 2803–2809 (2007).

[156] P. W. Milonni and J. H. Eberly, *Lasers* (Wiley, 1988), Sect. 14.7.

[157] J. I. Gersten, R. R. Alfano, and M. Belic, "Combined stimulated raman scattering and continuum self phase modulation," Phys. Rev. A **21**, 1222-1224 (1980).

[158] S. A. Diddams, L. Hollberg, and V. Mbele, "Molecular fingerprinting with the resolved modes of a femtosecond laser frequency comb," *Nature* **445**, 0028-0836 (2006).

[159] M. J. Thorpe, D. B. Clausen, M. S. Kirchner and J. Ye, "Cavity-enhanced optical frequency combspectroscopy: application to human breathanalysis," *Opt. Express* **16**, 2387–2397 (2008).

[160] A. Labruyére, A. Tonello, V. Couderc, G. Huss and P. Leproux "Compact supercontinuum sources and their biomedical applications," *Opt. Fiber Technol.***18**, 375–378 (2012).

[161] H. Imam, "Metrology: Broad as a lamp, bright as a laser," *Nat. Photonics* **2**, 26–28 (2008).

[162] S. V. Smirnov, J. D. Ania-Castanon, T. J. Ellingham, S. M. Kobtsev, S. Kukarin, and S. K. Turitsyn, "Optical spectral broadening and supercontinuum generation in telecom applications," *Opt. Fiber Technol. China* **12**, 122–147 (2006).

[163] M. Erkintalo, M. Surakka, J. Turunen, A. T. Friberg, and G. Genty, "Coherent-mode representation of supercontinuum," *Opt. Lett.* **37**, 169–171 (2012).

[164] J. M. Dudley, G. Genty, and S. Coen, "Supercontinuum generation in photonic crystal fiber," *Rev. Mod. Phys.* **78**, 1135–1184 (2006).

[165] M. Korhonen, A. T. Friberg, J. Turunen, and G. Genty, "Elementary field representation of supercontinuum," *J. Opt. Soc. Am. B* **30**, 21–26 (2013).

[166] J. W. Goodman, *Statistical Optics* (Wiley, 2000).

[167] H. H. Hopkins, "On the diffraction theory of optical images," *Proc. Roy. Soc. London A* **217**, 408–432 (1953).

[168] B. Möller, "Imaging of a straight edge in partially coherent illumination in the presence of spherical aberrations," *Opt. Acta* **15**, 223–236 (1968).

[169] S. B. Mehta, C. J. R. Sheppard, "Equivalent of the point spread function for partially coherent imaging," *J. Mod. Opt.* **57**, 718–739 (2010).

[170] K. Yamazoe, "Two models for partially coherent imaging," *J. Opt. Soc. Am. A* **29**, 2591–2597 (2012).

[171] E. C. Kintner, "Method for the calculation of partially coherent imagery," *Appl. Opt.* **17**, 2747–2753 (1978).

[172] J. van der Gracht, "Simulation of partially coherent imaging by outer-product expansion," *Appl. Opt.* **17**, 3725–3731 (1994).

[173] K. Yamazoe, "Computation theory of partially coherent imaging by stacked pupil shift matrix," *J. Opt. Soc. Am. A* **25**, 3111–3119 (2008).

[174] S. B. Mehta and C. J. R. Sheppard, "Phase-space representation of partially coherent imaging using the Cohen class distribution," *Opt. Lett.* **35**, 348–350 (2010).

[175] A. E. Rosenbluth, S. J. Bukofsky, M. Hibbs, K. Lai, R. N. Singh and A. K. K. Wong, "Optimum mask and source patterns to print a given shape," *J. Micro/Nanolith., Microfab., Microsyst.* **1**, 13–30 (2002).

[176] R. L. Gordon and A. E. Rosenbluth, "Lithographic image simulation for the 21st century with 19th-century tools," *Proc. SPIE* **5182**, 73–87 (2003).

[177] R. L. Gordon, "Exact computation of scalar, 2D aerial imagery," *Proc. SPIE* **4692**, 517–531 (2002).

[178] B. E. A. Saleh and M. Rabbani, "Simulation of partially coherent imagery in the space and frequency domains and by modal expansion," *Appl. Opt.* **21**, 2770–2777 (1982).

[179] A. S. Ostrovsky, O. R. Romero and M. V. R. Solís, "Coherent-mode representation of partially coherent imagery," *Opt. Rev.* **3**, 492–496 (1996).

[180] A. S. Ostrovsky and C. R. Parrao, "Fast algorithm for computer simulation of optical systems with partially coherent illumination," *2nd WSEAS Int. Conf. C. E. A*, 25–27 (2008).

[181] T. Voipio, T. Setälä, and A. Friberg, "Coherent-mode representation of partially polarized pulsed electromagnetic beams," *J. Opt. Soc. Am. A* **30**, 2433 (2013).

[182] Y. Li, J. Guo, L. Liu, T. Wang, and J. Shao, "Linear equations method for modal decomposition using intensity information," *J. Opt. Soc. Am. A* **30**, 2502–2509 (2013).

[183] J. Aun, F. Valdivia-Valero, and M. Nieto-Vesperinas, "Optical binding of cylinder photonic molecules in the near field of partially coherent fluctuating Gaussian Schell model sources: a coherent mode representation," *J. Opt. Soc. Am. A* **31**, 206–216 (2014).

[184] R. Martnez-Herrero, P. M. Mejas, and F. Gori, "Genuine cross-spectral densities and pseudo-modal expansions," *Opt. Lett.* **34**, 1399–1401 (2009).

[185] T. J. Skinner, "Surface texture effects in coherent imaging," *J. Opt. Soc. Am.* **53**, 1350A (1963).

[186] P. S. Considine, "Effects of coherence in imaging systems," *J. Opt. Soc. Am.* **56**, 1001–1009 (1966).

[187] W. T. Welford,*Aberrations of Optical Systems* (CRC Press, 1986).

[188] D. S. Goodman and A. E. Rosenbluth,"Condenser aberrations in Köhler illumination," *Proc. SPIE* **922**, 108–134 (1988).

[189] S. Subramanian, "Rapid calculation of defocused partially coherent images," *Appl. Opt.* **20**, 1854–1857 (1981).

[190] E. Noponen, A. Vasara, J. Turunen, J. M. Miller, and M. R. Taghizadeh, "Synthetic diffractive optics in the resonance domain," *J. Opt. Soc. Am. A* **9**, 1206-1213 (1992)

[191] E. Noponen, J. Turunen, and F. Wyrowski, "Synthesis of paraxial-domain diffractive elements by rigorous electromagnetic theory," **12**, 1128-1133 (1995).

[192] J. Turunen, M. Kuittinen, and F. Wyrowski, "Diffractive optics: electromagnetic approach," Progr. Opt **40**, E. Wolf, ed. (Elsevier, Amsterdam, 2000), 341–387.

[193] L. Novotny and B. Hecht, *Principles of Nano-Optics* (Cambridge University Press, Cambridge, 2006).

[194] H. Kim, J. Park, and B. Lee, *Fourier Modal Method and Its Applications in Computational Nanophotonics* (CRC Press, 2012).

Manisha Singh

Partially coherent beam shaping and imaging

The thesis contributes new results to the theory of partially coherent light and its applications to beam shaping and imaging problems that are of central importance in modern photonics research. Techniques are introduced for shaping the spatial intensity distributions of both beams and pulse trains originating from partially coherent light sources into a more desirable form. Numerically efficient methods for analyzing the effects of partial coherence in imaging problems (including microscopy) are also developed.

UNIVERSITY OF
EASTERN FINLAND

Publications of the University of Eastern Finland

Dissertations in Forestry and Natural Sciences

ISBN: 978-952-61-1998-4 (printed)

ISSN: 1798-5668

ISBN: 978-952-61-1999-1 (pdf)

ISSN: 1798-5676